J. Fluid Mech. (1988), *vol.* 195, *pp.* 303–340
Printed in Great Britain

Symmetric vortex merger in two dimensions: causes and conditions

By M. V. MELANDER,† N. J. ZABUSKY†
AND J. C. McWILLIAMS‡

† Institute for Computational Mathematics and Applications, Department of Mathematics and Statistics, University of Pittsburgh, Pittsburgh, PA 15260, USA

‡ National Center for Atmospheric Research, P.O. Box 3000 Boulder, CO 80307-3000, USA

(Received 6 October 1986 and in revised form 16 February 1988)

Two like-signed vorticity regions can pair or merge into one vortex. This phenomenon occurs if the original two vortices are sufficiently close together, that is, if the distance between the vorticity centroids is smaller than a certain critical merger distance, which depends on the initial shape of the vortex distributions. Our conclusions are based on an analytical/numerical study, which presents the first quantitative description of the cause and mechanism behind the restricted process of symmetric vortex merger. We use two complementary models to investigate the merger of identical vorticity regions. The first, based on a recently introduced low-order physical-space moment model of the two-dimensional Euler equations, is a Hamiltonian system of ordinary differential equations for the evolution of the centroid position, aspect ratio and orientation of each region. By imposing symmetry this system is made integrable and we obtain a necessary and sufficient condition for merger. This condition involves only the initial conditions and the conserved quantities. The second model is a high-resolution pseudospectral algorithm governing weakly dissipative flow in a box with periodic boundary conditions. When the results obtained by both methods are juxtaposed, we obtain a detailed kinematic insight into the merger process. When the moment model is generalized to include a weak Newtonian viscosity, we find a 'metastable' state with a lifetime depending on the dissipation timescale. This state attracts all initial configurations that do not merge on a convective timescale. Eventually, convective merger occurs and the state disappears. Furthermore, spectral simulations show that initial conditions with a centroid separation slightly larger than the critical merger distance initially cause a rapid approach towards this metastable state.

1. Introduction

In a series of papers, we have investigated the evolution of one or two isolated vorticity regions (Melander, McWilliams & Zabusky 1987*a*; Melander, Zabusky & McWilliams 1987*b*). This study is of paramount importance for a deeper understanding of two-dimensional turbulence, partly because like-signed vortex regions in a decaying turbulent flow merge or 'agglomerate' into increasingly larger vortices (McWilliams 1984). This concentration of vorticity takes place through mergers of individual vortex regions – hence the importance of the merger process. The immediate result of a merger is an elongated compound vortex core. This core quickly tends towards a circularly symmetric state because, as we showed in the first paper (Melander *et al.* 1987*a*), a single-signed sufficiently eccentric vortex relaxes towards axisymmetry (circular symmetry) on a circulation timescale owing to an inviscid mechanism.

The first clear experimental evidence for merger was given by Freymuth (1966) in photographs of streamlines in a free-shear layer. Later Winant & Browand (1974) and Brown & Roshko (1974) gave more quantitative evidence. Computationally, Roberts & Christiansen (1972) observed merger of two localized regions using a two-dimensional vortex-in-cell code with periodic boundary conditions. This process was also observed by Zabusky & Deem (1971), Christiansen & Zabusky (1973) and Rossow (1977). Zabusky & Deem studied several initial conditions that model aspects of a von Kármán wake at moderate Reynolds number and observed that energy cascade into lower wavenumbers was consistent with a decrease in the number of extrema of the pressure contours. The clearest early example was given by Christiansen & Zabusky, who modelled aspects of the von Kármán street at high Reynolds number with the vortex-in-cell code. They initialized a non-symmetric 'street' of two positive and two negative regions of vorticity and observed a variety of parameter regions that lead to vortex merger. Zabusky, Hughes & Roberts (1979) obtained the critical separation distance for merger of two circular vortex regions with uniform vorticity and equal radii in a numerical study using a contour dynamics (CD) representation of the Euler equations. Overman & Zabusky (1982) presented a variety of CD calculations and showed that merger can result from an instability of an unstable steady corotating state. Dritschel (1986) used the CD representation and presented more detailed evidence that the merger of two nearly stationary vortices depends on the configuration's linear stability.

In spite of its importance, there has been little basic understanding of why the merger process occurs. We claim that the process is an 'axisymmetrization' process driven by filament formation. The symmetric merger phenomenon to which this paper is devoted is physically a rare occurrence, but mathematically its simplified nature is convenient. In fact, the symmetry makes the second-order moment model (Melander, Zabusky & Styczek 1986) integrable. Although the model is based on the assumption that the vortices are well-separated and therefore becomes increasingly invalid during a merger, the model yields a good description of the initial stages of evolution towards a merger. Most important, we obtain from the model an explicit condition for the threshold to merger. In the case of nearly circular vortices (aspect ratio < 2.3) this merger condition involves only the 'excess' energy and the angular impulse.

We emphasize the use of 'complementary modelling' as a mode of study for this nonlinear dynamical problem. Namely, we use a pseudospectral algorithm as a faithful representation of the evolution of smooth vorticity distribution in a weakly dissipative two-dimensional fluid (e.g. §2), and we use the moment model as an analytically tractable low-order representation for obtaining analytical insights (§3). The results from these different models are juxtaposed in §§4 and 5. In §6 we examine the influence of dissipation on the merger process using the same complementary modelling approach.

2. A high-resolution simulation of a symmetric merger

Vortex dynamics in two dimensions can be described by the following equations governing the evolution of the vorticity and stream function:

$$d_t\omega \equiv \omega_t+\omega_x\psi_y-\omega_y\psi_x = \nu_2\Delta\omega-\nu_4\Delta^2\omega, \tag{1}$$

$$\Delta\psi = -\omega. \tag{2}$$

Here ν_2 is the traditional Newtonian viscosity and ν_4 is a hyperviscosity frequently used in spectral models. (When $\nu_2 = \nu_4 = 0$, we have the two-dimensional Euler equations). In this section we discuss a numerical solution of (1) and (2) with $\nu_2 = 0$ and $\nu_4 \neq 0$. The simulation is performed with a pseudospectral code (Haidvogel 1985) which solves (1) and (2) in the periodic domain $[-\pi, \pi] \times [-\pi, \pi]$. We initialize with two isolated smooth vortex distributions of compact support. Each distribution is specified in a polar coordinate system (r, ϕ) centred at the distribution's centroid. The equivorticity lines of each of these vortices are concentric ellipses with a common orientation and aspect ratio. Outside the ellipse $r = R_0(\phi)$ there is no vorticity and inside $r = R_i(\phi)$ the vorticity is uniform, $\omega = \omega_p$. The relative steepness of the vorticity gradient is given by the parameter $\delta = (R_0 - R_i)/R_0$. We refer to such a vorticity distribution as $V(\delta, \omega_p, a, b)$, where a and b are the major and minor axis of the outermost ellipse $r = R_0(\phi)$. We have found it convenient to specify $\omega(r, \phi)$ as a distribution with a monotone profile function $f(r), r > 0$.

$$\omega(r,\phi) = \omega_p \begin{cases} 1, & r \leqslant R_i(\phi), \\ 1 - f[(r - R_i(\phi))/(R_0(\phi) - R_i(\phi))], & R_i(\phi) \leqslant r < R_0(\phi), \\ 0, & R_0(\phi) < r. \end{cases} \tag{3}$$

We select our profile function f from the one-parameter family $\{f_k\colon k > 0\}$, where

$$f_k(r) = \exp\left[\left(\frac{-k}{r}\right)\exp\left(\frac{1}{r-1}\right)\right], \quad 0 < r < 1. \tag{4}$$

This function smoothly connects levels 0 and 1 at $r = 0$ and $r = 1$, and all its derivatives vanish at these points. A suitable k is obtained from the natural requirement that $f(0.5) = 0.5$, and this implies that $k = 2.56085$. With this choice of k we find $f'(0.5) = \ln 8 \approx 2.08$, and approximately 90% of the variation of the function f occurs within the interval $(0.25, 0.75)$.

Figure 1 shows the evolution of two smooth initially circular vortices, specifically two $V(1, 20, 0.9, 0.9)$ vortices with an initial centroid separation of 1.35. This centroid separation is well below the critical merger separation which guarantees a quick merger. The simulation is performed on a 256^2 mesh with $\nu_4 = 4.0 \times 10^{-8}$ until $t = 4.0$. From there on the calculation is done on a 128^2 mesh with $\nu_4 = 50.0 \times 10^{-8}$ until $t = 8.0$. Panel (ω) shows the evolution of the vorticity field. Panel (ψ) shows the corresponding stream function. This simulation represents a typical symmetric merger. It is evident from figure 1 that a nearly axisymmetric monopole is produced on a circulation timescale. On the basis of simulations like this one, we claim that (symmetric) merger is an inviscid axisymmetrization process. In fact, it is quite similar to the process in which a non-circular monopole tends towards circular symmetry on a convective timescale (Melander *et al.* 1987*a*). In order to see this similarity clearly we introduce a corotating stream function ψ_c:

$$\psi_c(x, y; t) \equiv \psi(x, y; t) - \tfrac{1}{2}(x^2 + y^2)\,\Omega(t), \tag{5}$$

where $\Omega(t)$ denotes a characteristic angular velocity for the rotation of the entire vorticity configuration around the common vorticity centroid. As discussed in Melander *et al.* (1987*a*), we have not found a unique or best way of defining Ω (except for corotating steady states). A reasonable Ω is obtained by first fitting an ellipse to a *streamline* near the edge of the vortex core, in order to define the orientation of the entire configuration. Ω is then obtained by differentiating the orientation of the

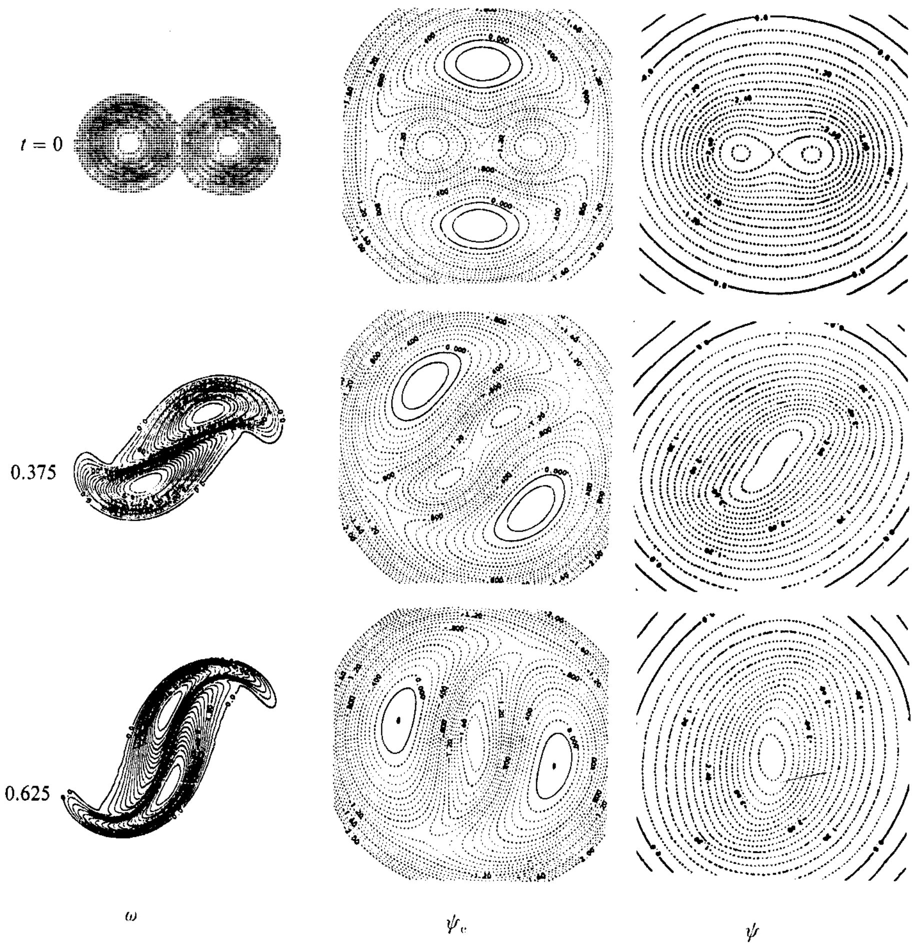

FIGURE 1 (Part 1). For caption see facing page.

major axis with respect to time. Using this Ω in (5) yields the corotating stream function displayed in panel (ψ_c) of figure 1. The comparison of the panels (ω) and (ψ_c) immediately justifies the introduction of the corotating stream function, because we observe that the vorticity configuration deforms and spins off arms of vorticity (filaments) in accord with the structure of the corotating stream function ψ_c (as described in great detail in Melander *et al.* 1987*a*).

The corotating stream function ψ_c clearly has more closed streamlines and stagnation points than the original stream function. The introduction of a rotating reference frame gives rise to two fictitious vortices, which we shall call *ghost vortices*. It is instructive to compare the structure of ψ_c for a single elliptical vortex with the structure of ψ_c for two nearby vortices. Figure 2 shows a qualitative sketch of the differences. For the two-vortex configuration, shown in figure 2(*a*), we observe seven stagnation points, three saddle points and four centres. The separatrices connecting the saddle points divide the plane into six regions. Of special interest are the ghost vortices G_1 and G_2. Their existence is associated with the ellipticity of the global vorticity distribution, as seen by comparing with the corotating stream function field for a single ellipse (figure 2*b*). The ghost vortices can give rise to the generation of

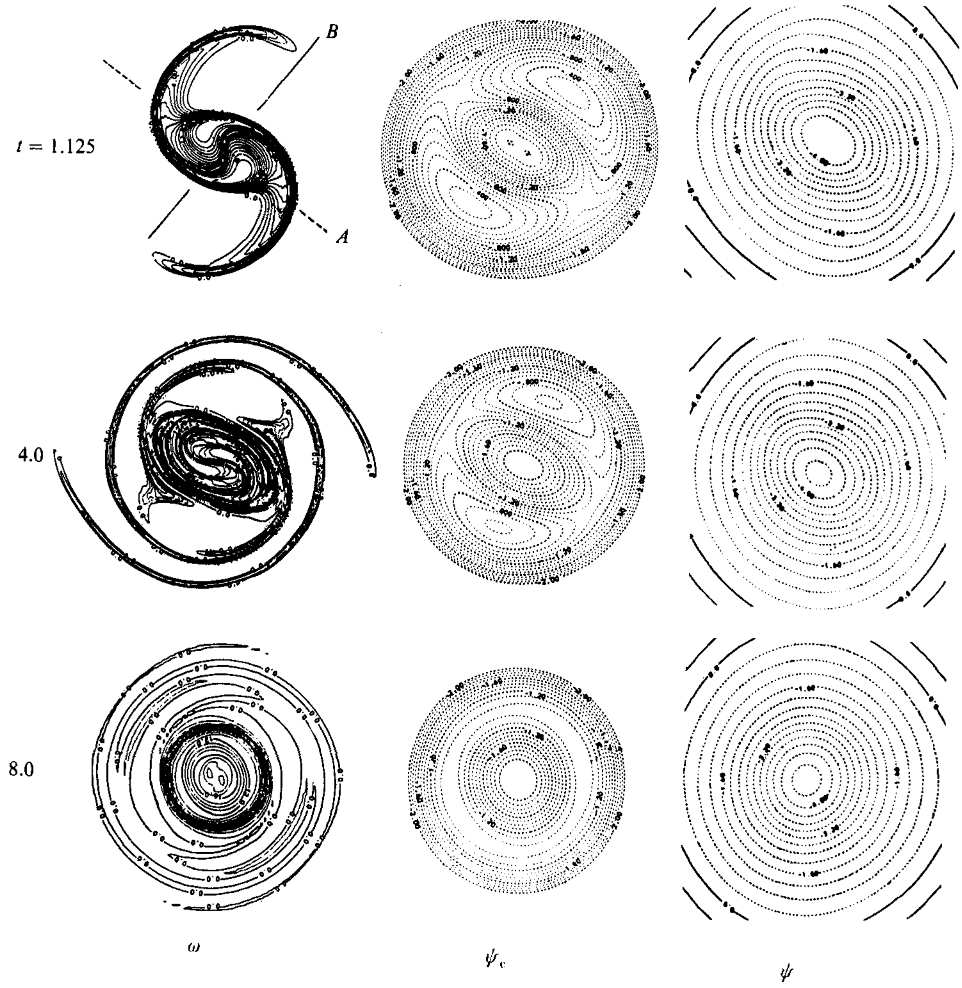

FIGURE 1. Simulation of the evolution of two smooth initially circular vortices $V(1, 20, 0.9, 0.9)$, with an initial centroid separation of 1.35. The panels at $t = 0, t = 0.375, t = 0.625, t = 1.125$, $t = 4.0, t = 8.0$ show the vorticity field (ω), the stream function (ψ) and the corotating stream function (ψ_c) as defined in (5). For $t \leqslant 4.0$ the simulation was performed on a 256^2 mesh with $\nu_4 = 4 \times 10^{-8}$ and for $t \geqslant 4.0$ on a 128^2 mesh with $\nu_4 = 5 \times 10^{-7}$.

vorticity filaments along the separatrices labelled o_1 and o_2, as described in our paper on the evolution of a single elliptical vortex (Melander *et al.* 1987*a*). The qualitative difference between the corotating stream function fields for one and two vortices is found in the region between the separatrices labelled i_1 and i_2; this region we name the compound core region. Inside the compound core region we identify two individual core regions C_1 and C_2. Also we observe ψ_c streamlines surrounding both C_1 and C_2. These ψ_c streamlines occupy a band (shaded in figure 2*a*), which we designate the *exchange* band ($\mathscr{E}$-band) since it allows the two vortices to exchange vorticity. The $\mathscr{E}$-band exists for all corotating equilibria as discussed in Dritschel (1985). During the evolution shown in figure 1 we observe that ψ_c changes its structure from a two-vortex structure of the type sketched in figure 2(*a*) to a one-vortex structure of the type sketched in figure 2(*b*). This change takes place when the

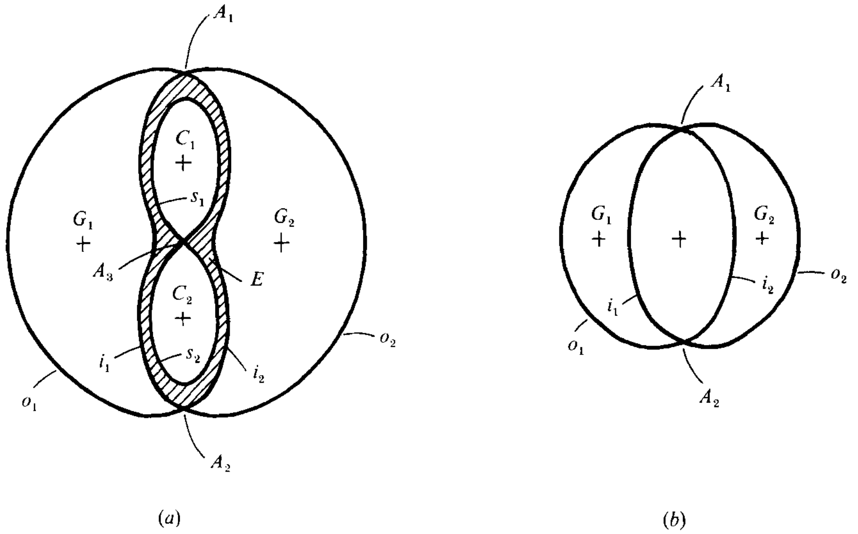

(a) (b)

FIGURE 2. Sketch of the corotating stream function for: (a) a two-vortex configuration; (b) an elliptical vortex.

two centres approach the saddle A_3 to form a single centre through a centre–saddle annihilation.

The $\mathscr{E}$-band is essential for a heuristical understanding of the close interaction of two vortices. We identify three characteristically different evolutions corresponding to the three different vorticity distributions relative to the $\mathscr{E}$-band. First, if the vorticity is confined to the individual core regions C_1 and C_2, we expect the two vortices to circle around each other endlessly without ever exchanging vorticity or merging. Clearly, this case occurs when the two vortices are far apart. Second, if the vorticity is confined to the individual core regions and the $\mathscr{E}$-band, we expect the two vortices to circle each other while exchanging the vorticity in the $\mathscr{E}$-band; however, we *do not* expect filament generation and merger. An example of two vortices exchanging vorticity without merging is shown in figure 12. Third, if the vorticity distribution extends to regions outside the $\mathscr{E}$-band, we expect the vorticity configuration to eject filaments and undergo merger. The evolution shown in figure 1 serves as an example. Although all three evolutions can occur and the juxtaposition of the ψ_c and ω-fields offers a simple heuristic explanation of each case, we cannot consider this discussion as more than a guide for our physical intuition because ψ_c changes with ω, and $\Omega(t)$ is not a well-defined quantity.

The initial condition in figure 1 is selected such that there is sufficient vorticity outside the $\mathscr{E}$-band for a quick merger. We observe that the vorticity in the $\mathscr{E}$-band is advected and a steep-gradient interface is formed between the two vortices at $t = 0.375$. Owing to the symmetry in the initial conditions this interface passes exactly through the common vorticity centroid and will be present there until it is erased by dissipation. We also observe that the $\mathscr{E}$-band is growing at the expense of the individual core regions C_1 and C_2. This is evident at $t = 0.375$, and at $t = 0.625$ the individual core regions have disappeared entirely and the $\mathscr{E}$-band has become the core region of a single vortex.

At $t = 1.125$ most particles carrying low-amplitude vorticity have been advected into the filaments, thereby intensifying the vorticity gradients near the core as shown

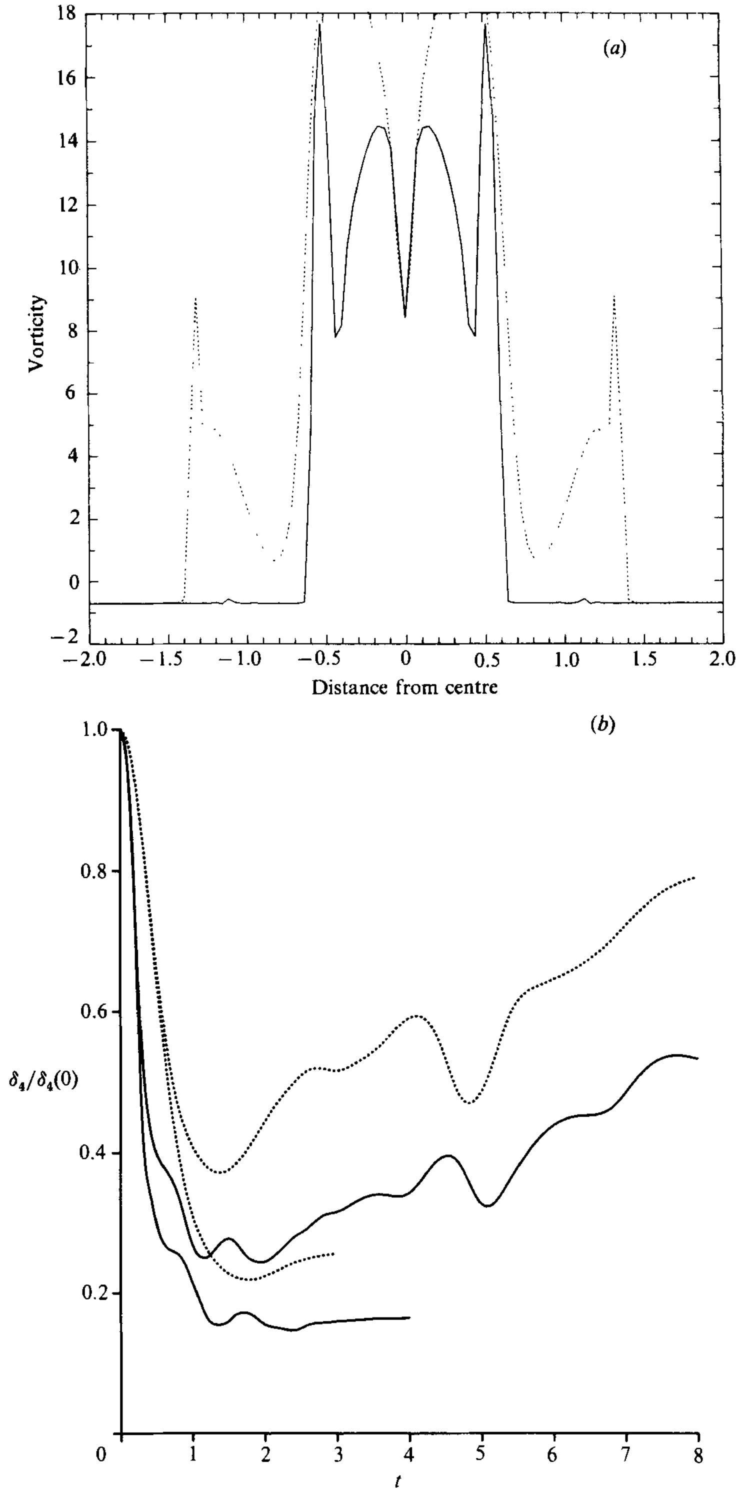

FIGURE 3. (*a*) Two cross-sections of the vorticity field at $t = 1.125$ along the two perpendicular axes A and B shown in figure 1. (A dotted line, B solid line.) The maximum vorticity is 20.0. (*b*) The characteristic lengthscale $\delta_4/\delta_4(0)$ versus time for the merger simulation of figure 1 (——) and for the axisymmetrization simulation (····) in figure 8 of Melander *et al.* (1987*a*). The upper and lower curves in each set correspond to 128^2 and 256^2 simulations, respectively.

in the cross-sections displayed in figure 3(*a*). Since both vortices have contributed vorticity to each filament, the filaments look like two nearby thin vortex layers with adjacent steep-gradient interfaces.

Inside the new compound vortex core there is a strong differential rotation. The fastest rotation occurs at the centre while the filaments rotate more slowly. Owing to this differential rotation the length of the interface between the original two vortices increases. The gradients across this interface thereby maintain their steepness for a long time in spite of the dissipation. This can be appreciated by considering the corresponding inviscid problem. Here, the distances between the two vorticity regions decrease as the length of the interface between them increases (Kelvin's theorem). However, with dissipation there is a competition and although the region between the vorticity regions is 'filled' by diffusion, the steepness is maintained because the interface lengthens.

In order to diagnose this competition we define a lengthscale δ_4 which characterizes the enstrophy cascade in (1) and (2)

$$\delta_4 \equiv \left[\frac{\int |\Delta\omega|^2 \,\mathrm{d}x\,\mathrm{d}y}{\int \omega^2 \,\mathrm{d}x\,\mathrm{d}y}\right]^{-\frac{1}{4}}.$$

It is easy to show that with $\nu_2 = 0, \nu_4 \neq 0$, δ_4 is related to the enstrophy dissipation through the following power law:

$$2\nu_4 Z \Big/ \left(\frac{\mathrm{d}Z}{\mathrm{d}t}\right) = -\delta_4^4,$$

where Z is the enstrophy, $Z = \int \omega^2 \,\mathrm{d}x\,\mathrm{d}y$ (see Appendix A).

In figure 3(*b*) we see the variation of $\delta_4(t)/\delta_4(0)$ at two different resolutions, 128^2 and 256^2. In each set there are two curves, a dashed one for the axisymmetrization of a single region of vorticity $V(1, 20, 1.6, 0.8)$ (the evolution is shown in Melander *et al.* 1987*a*) and a solid curve for the merger of two regions of vorticity with initial conditions as in figure 1. The merger curve is initially below the axisymmetrization curve, indicating a stronger enstrophy cascade. The gradual upturn of the 128^2 curve shows that the dissipation process decreases gradients slowly. However, the fact that the merger curve remains below the axisymmetrization curve and grows more slowly (on the average) indicates a strong competition between gradient intensification and dissipation. The slight downturn in both curves at $t \approx 4.5$ is due to formation of secondary filaments, as discussed in Melander *et al.* (1987*a*), §4.1.

3. An integrable model of the symmetric merger process

In the previous section we examined a high-resolution numerical simulation of a symmetric merger. We shall now adopt a complementary modelling approach. Instead of resolving the process in all details we seek a model that is as simple as possible and still allows the merger process to occur. Although this model will ignore most of the details, it can provide important knowledge of the basic physics and the essential variables in the process. Since our understanding of the merger process is still imperfect (Aref 1983), a simple integrable model of this process should be most welcome.

The well-known point-vortex model does not provide an integrable model of the merger process, i.e. two point vortices of equal strength circle around the common vorticity centroid and never merge. This is because the Hamiltonian, which is constant in time, involves only one combination of the variables, namely, the distance between the point vortices. If we use more point vortices to model the problem more realistically we lose the integrability (Aref 1983). The only known model of the two-dimensional Euler equations that yields an integrable model of the symmetric merger is the Hamiltonian moment model of Melander *et al.* (1986). In the following, we investigate how this model applies to symmetric merger. For the sake of completeness, we briefly present the moment model.

3.1. *The moment-model equations*

The moment model is a low-order representation of the two-dimensional Euler equations, which govern the evolution of well-separated uniform vortices. The two-dimensional Euler equations have a weak integral formulation in terms of an arbitrary test function F, namely

$$d_t \iint_{\mathbb{R}^2} F(x,y)\,\omega(x,y,t)\,\mathrm{d}x\,\mathrm{d}y = \iint_{\mathbb{R}^2} \omega(x,y,t)\,[F_x \psi_y - F_y \psi_x]\,\mathrm{d}x\,\mathrm{d}y, \tag{6}$$

$$\psi(x,y,t) = -\frac{1}{4\pi}\iint_{\mathbb{R}^2} \omega(\xi,\eta,t)\,\ln\left((x-\xi)^2+(y-\eta)^2\right)\mathrm{d}\xi\,\mathrm{d}\eta. \tag{7}$$

We assume that the vorticity is located in N regions $D_k, k = 1,2,\ldots,N$. If these regions are well separated, elliptical and each has constant vorticity (i.e. in isolation each vortex is a Kirchhoff ellipse), then ψ is well-approximated by a quadratic polynomial in each region D_k. If we restrict the test functions F to those functions that are quadratic in the vorticity regions, then (6) becomes a closed system for the evolution of the physical space moments,

$$J_k^{mn} = \iint_{D_k} \omega(x,y,t)\,x^m y^n\,\mathrm{d}x\,\mathrm{d}y, \tag{8}$$

up to the second order, or $m+n \leqslant 2$. Each vorticity region D_k is then characterized by its centroid position (x_k, y_k), its vorticity ω_k, area A_k orientation ϕ_k and aspect ratio λ_k. The moment-model equations can be expressed as $4N$ equations for the evolution of $x_k, y_k, \phi_k, \lambda_k, k = 1,2,\ldots,N$ as shown in Melander *et al.* (1986). In these equations, ω_k and A_k appear as constants. The moment-model equations conserve the following: the global vorticity centroid

$$X \equiv \sum_{k=1}^{N} A_k \omega_k x_k \Big/ \sum_{k=1}^{N} A_k \omega_k \tag{9}$$

and

$$Y \equiv \sum_{k=1}^{N} A_k \omega_k y_k \Big/ \sum_{k=1}^{N} A_k \omega_k; \tag{10}$$

the total angular impulse

$$M \equiv \iint \omega(x,y)\,(x^2+y^2)\,\mathrm{d}x\,\mathrm{d}y = \sum_{k=1}^{N} \omega_k A_k \left[x_k^2 + y_k^2 + \frac{A_k}{4\pi}\frac{1+\lambda_k^2}{\lambda_k}\right]; \tag{11}$$

and the excess energy

$$\begin{aligned} H \equiv -\frac{1}{2}\iint \omega\psi \,\mathrm{d}x\,\mathrm{d}y = -\sum_{k=1}^{N} \Bigg\{ & \frac{A_k^2\,\omega_k^2}{8\pi}\ln\left(\frac{(1+\lambda_k)^2}{4\lambda_k}\right) - \frac{A_k^2\,\omega_k^2}{16\pi} \\ & + \sum_{\alpha=1}^{N}{}' \frac{\omega_\alpha A_\alpha \omega_k A_k}{8\pi} \ln\left((x_k-x_\alpha)^2+(y_k-y_\alpha)^2\right) \\ & + \sum_{\alpha=1}^{N}{}' \frac{\omega_\alpha A_\alpha \omega_k A_k}{32\pi^2((x_k-x_\alpha)^2+(y_k-y_\alpha)^2)^2} \\ & \times \Bigg[A_\alpha \frac{(1-\lambda_\alpha^2)}{\lambda_\alpha} (((x_k-x_\alpha)^2-(y_k-y_\alpha)^2)\cos 2\phi_\alpha \\ & + 2(x_k-x_\alpha)(y_k-y_\alpha)\sin 2\phi_\alpha) \\ & + A_k \frac{(1-\lambda_k^2)}{\lambda_k} (((x_k-x_\alpha)^2-(y_k-y_\alpha)^2)\cos 2\phi_k \\ & + 2(x_k-x_\alpha)(y_k-y_\alpha)\sin 2\phi_k) \Bigg] \Bigg\}. \end{aligned} \tag{12}$$

The moment model is an asymptotic expansion with an error of $O(\epsilon^3)$ in the parameter

$$\epsilon \equiv \frac{\text{max diameter } D_k}{\text{min centroid separation}}. \tag{13}$$

The model becomes increasingly invalid if two vortex regions approach closely, because in that case each region will quickly depart from an ellipse, as shown for example by Overman & Zabusky (1982). Also, the stream function becomes increasingly less well described by a quadratic polynomial inside such vorticity regions.

However, asymptotic expansions have often proven accurate and useful for quite large values of the expansion parameter. Experiments shows that this is also the case for the moment model. Of particular importance for this paper is the fact the moment model has its own 'merger' process. That is, if initially two elliptical regions are sufficiently close together, as in figure 4, and evolve according to the moment-model equations, then their intercentroid distance decreases and vanishes in a finite time, a process we call 'collapse'. We have found good agreement between critical collapse distances of the moment model and critical merger distances of two-dimensional Euler equations. The difference is of the order 5–10%. For example, the critical merger intercentroid distance for two identical piecewise-constant circular vortices is $3.4(A/\pi)^{\frac{1}{2}}$ while the critical collapse intercentroid distance is $3.2(A/\pi)^{\frac{1}{2}}$ (here A is the area of each vortex). On the basis of these observations we conclude that collapse in the moment model is relevant for investigating the merger phenomenon.

Figure 5 shows the geometrical configuration for the symmetric merger problem. The common vorticity centroid is taken as the origin of a Cartesian system. The two ellipses are situated symmetrically around the origin. Clearly, the configuration is described by four variables, the polar coordinates of the centre of one ellipse (R, θ),

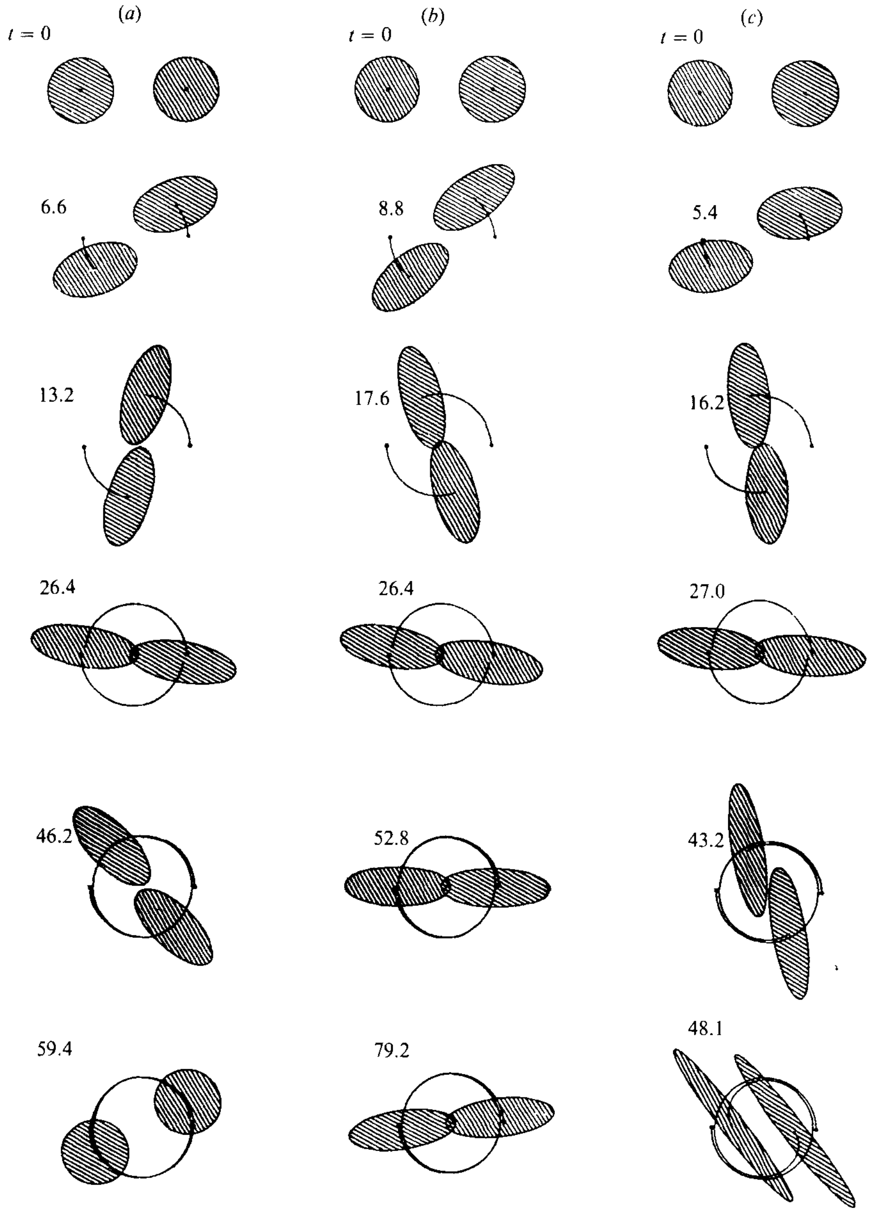

FIGURE 4. Examples of the moment model's ability to distinguish between merger and non-merger. The initial conditions in all three panels are uniform circular vortices with radius 1 but slightly different centroid separation: (*a*) $D = 3.202000$, (*b*) $D = 3.201520$, (*c*) $D = 3.20000$. The centroid trajectory of each vortex centroid is also shown. We observe that the moment-model analogue of a merger is a collapse in which the centroids coincide in a finite time. Also we observe that collapse (*c*) and non-collapse (*a*) are separated by an unstable steady state (*b*). Although the assumptions on which the moment model are based breakdown during a collapse, it is clear from these three panels that the moment model is able to distinguish between merger and non-merger.

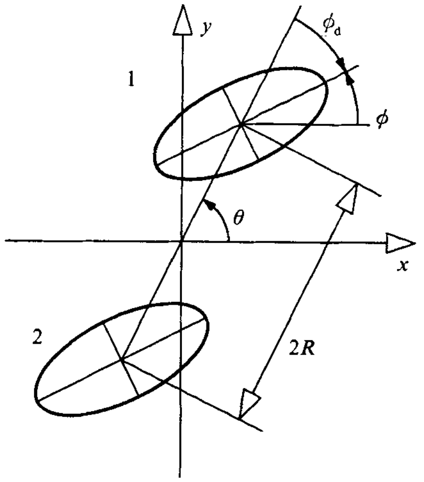

FIGURE 5. A sketch of two elliptical vortices symmetrically situated around the common vorticity centroid. The centroid of vortex 1 has the polar coordinates (R, θ) and the major axis is tilted by the angle ϕ. In a frame rotating with angular velocity $d_t \theta$ the orientation of the major axis is ϕ_d.

the aspect ratio λ and orientation ϕ of the ellipses. In terms of these variables the moment-model equations are

$$\dot{\lambda} = \frac{\lambda \omega A}{4\pi R^2} \sin 2(\theta - \phi), \tag{14}$$

$$\dot{\phi} = \frac{\omega \lambda}{(1+\lambda)^2} + \frac{\omega A(1+\lambda^2)}{8\pi R^2(1-\lambda^2)} \cos 2(\theta - \phi), \tag{15}$$

$$\dot{\theta} = A \frac{\omega}{4\pi R^2}\left[1 + \frac{A(\lambda^2-1)}{8\pi R^2 \lambda} \cos 2(\theta - \phi)\right], \tag{16}$$

$$\dot{R} = \frac{A^2 \omega (1-\lambda^2)}{32\pi^2 \lambda R^3} \sin 2(\theta - \phi), \tag{17}$$

where A and ω are constants. These equations are derived in Melander *et al.* (1986). We make these equations dimensionless by measuring time in units of ω^{-1} and length in units of $(A/\pi)^{\frac{1}{2}}$. Hence the normalized equations are obtained by setting $\omega = 1$ and $A = \pi$ in (14)–(17). A convenient normalization of the angular impulse is

$$\sigma \equiv 2\pi M / \omega A^2, \tag{18}$$

where, as seen from (11), $\sigma \geqslant 2$ with $R > 0$ and $\lambda \geqslant 1$.

3.2. *The complete solution of the model equations*

It is apparent from (14)–(17) that the angle variables appear only in the combination $\phi_d \equiv \phi - \theta$. Furthermore, since we have two conservation laws, $\dot{M} = \dot{H} = 0$, the equations (14)–(17) form an integrable system. The conservation law for angular impulse, $\dot{M} = 0$, may be used to eliminate R with

$$K \equiv \frac{1}{4R^2} = \frac{1}{\sigma - (1+\lambda^2)/\lambda}. \tag{19}$$

Thereby, we can express the system in terms of ϕ_{d} and λ, or

$$\dot{\lambda} = -\lambda K \sin 2\phi_{\mathrm{d}}, \tag{20}$$

$$\dot{\phi}_{\mathrm{d}} = \Omega_{\mathrm{s}} - \Omega_{\mathrm{m}}, \tag{21}$$

where

$$\Omega_{\mathrm{s}} \equiv \frac{\lambda}{(\lambda+1)^2}, \tag{22}$$

$$\Omega_{\mathrm{m}} \equiv \tfrac{1}{2}K\left\{2+\left[\frac{\lambda^2+1}{\lambda^2-1}+\frac{K(\lambda^2-1)}{\lambda}\right]\cos 2\phi_{\mathrm{d}}\right\}. \tag{23}$$

Here Ω_{s} is the angular velocity of self-induced rotation of the Kirchhoff ellipse and Ω_{m} is the angular velocity produced by the neighbouring vortex. Hence the angular velocity of a vortex in the frame rotating with the two centroids is the result of a competition between mutual- and self-interaction.

The system (20) and (21) is autonomous. Hence for a fixed value of σ, a conserved quantity, the problem is within the framework of a classical phase-plane analysis. However, $(\lambda, \phi_{\mathrm{d}})$ is an inconvenient set of variables because there is a singularity in the equations for $\lambda = 1$, which is due to the way we describe the ellipse, namely, by an aspect ratio and an orientation. (Clearly, the orientation is not well defined for a circle.) There are other bad features of the $(\lambda, \phi_{\mathrm{d}})$-description as well. For example, the same ellipse can be described in many ways, $(\lambda, \phi_{\mathrm{d}})$, $(1/\lambda, \phi_{\mathrm{d}}+\frac{1}{2}\pi)$, etc. A convenient set of coordinates for the problem is

$$(D, G) \equiv \left(\frac{\lambda^2-1}{\lambda}\right)(\cos 2\phi_{\mathrm{d}}, \sin 2\phi_{\mathrm{d}}), \tag{24}$$

whereby each ellipse is uniquely represented and the equations are non-singular for $\lambda = 1$

$$\begin{pmatrix}\dot{D}\\ \dot{G}\end{pmatrix} = \left(K(2+KD)-\frac{2}{2+(4+D^2+G^2)^{\frac{1}{2}}}\right)\begin{pmatrix}G\\ -D\end{pmatrix}-\begin{pmatrix}0\\ K(4+D^2+G^2)^{\frac{1}{2}}\end{pmatrix}, \tag{25}$$

where

$$\frac{1}{K} = \sigma-(4+D^2+G^2)^{\frac{1}{2}}. \tag{26}$$

In terms of the new variables (D, G) the excess energy is

$$\begin{aligned} H &= \tfrac{1}{4}\pi[\tfrac{1}{2}DK-\ln([2+(4+D^2+G^2)^{\frac{1}{2}}]/4K)+\tfrac{1}{2}] \\ &= \tfrac{1}{4}\pi\left[\frac{(\lambda^2-1)}{8R^2\lambda}\cos 2\phi_{\mathrm{d}}-\ln\left(\frac{R^2(1+\lambda)^2}{\lambda}\right)+\tfrac{1}{2}\right]. \end{aligned} \tag{27}$$

The trajectories in the (D, G)-plane are the level curves of H.

3.3. *The merger condition*

Our interpretations are based on the (D, G)-phase plane. The origin in this plane represents circular vortex regions ($\lambda = 1$). As we move away from the origin λ increases and $R^2 \propto K^{-1}$ decreases, as seen from (24) and (26). R becomes zero on a circle C_0 of radius $(\sigma^2-4)^{\frac{1}{2}}$ and centre $(0, 0)$. Since the second-order moment model is a reasonable representation for the Euler equations only when the vortices are not too close, then evolution on this plane fails to describe a true merger as we approach the circle C_0. Equations (25) and (26) are reflection symmetric about the D-axis,

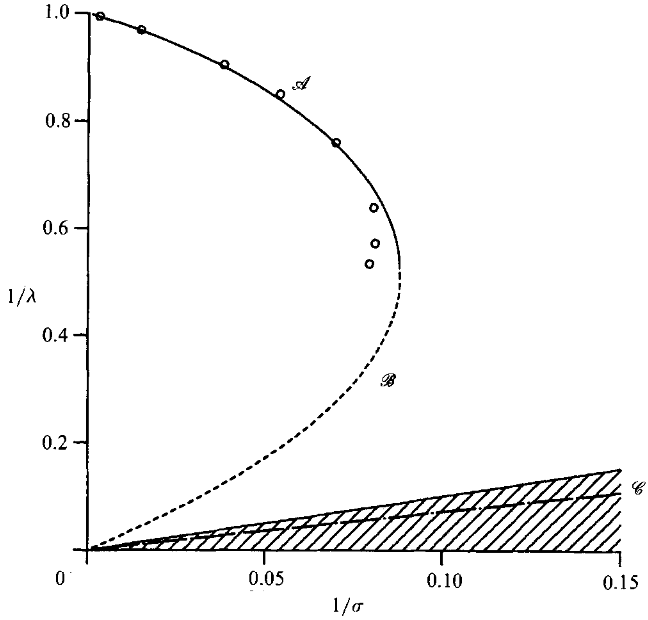

FIGURE 6. The inverse aspect ratio of the steady corotating states of the moment model is plotted versus the inverse dimensionless conserved quantity $\sigma = 2\pi M/\omega A^2$. 𝒜 (——) are centres and ℬ (– – – –) are saddle points. For the 𝒜 and ℬ states the major axes of the vortices are aligned. For a given value of σ the aspect ratio λ must be smaller than $\frac{1}{2}[\sigma + (\sigma^2-4)^{\frac{1}{2}}]$ in order to have a real non-vanishing centroid separation. The unphysical (hatched) region where this condition is not satisfied is shown. The polynomial (28) has one real root 𝒞 (–·–·–) in this region. The figure also shows results (○) from the steady-state contour-dynamical calculations of Overman & Zabusky (1982).

corresponding to time-reversal invariance. Furthermore, from (20) we note that the aspect ratio decreases when $G > 0$ and vice versa.

The steady-state solutions of (25) have been reported in Melander *et al.* (1986). The aspect ratio of the steady states are real roots of a fifth-order algebraic equation

$$4\lambda^5 - 7\sigma\lambda^4 + (2\sigma^2+\sigma+6)\lambda^3 - (2\sigma^2+3\sigma)\lambda^2 + 5\sigma\lambda - 8 = 0. \tag{28}$$

(In the previous work this equation was expressed in terms of the dimensionless centroid separation $\mu = 2R(\pi/A)^{\frac{1}{2}}$). Figure 6 shows the reciprocal aspect ratio λ^{-1} of the states as a function of σ^{-1}. There are one, two or three steady states depending on whether $\sigma < \sigma_{\mathrm{cr}} \approx 11.4$, $\sigma = \sigma_{\mathrm{cr}}$ or $\sigma > \sigma_{\mathrm{cr}}$. All of them are located on the D-axis. A local analysis shows that 𝒜 (solid) is a centre and ℬ (dashed) is a saddle point. 𝒞 corresponds to a solution outside the collapse circle that is without physical meaning. Let us consider the different values of σ in detail.

(*a*) $\sigma < \sigma_{\mathrm{cr}}$. Since there are no steady states for this value of σ, all trajectories must approach the circle C_0, as shown in figure 7. Since the energy remains constant as a trajectory approaches the circle C_0 (where $R = 0$) the singular terms in (27) are in balance. This implies that all trajectories approach one point on C_0 where $D = 0$ or $\cos 2\phi_{\mathrm{d}} = 0$ or $\phi_{\mathrm{d}} = -\frac{1}{4}\pi$. The corresponding point at $\phi_{\mathrm{d}} = +\frac{1}{4}\pi$ is the 'repeller' corresponding to time-reversal invariance.

(*b*) $\sigma = \sigma_{\mathrm{cr}}$. In this case we have one unstable steady state. All other trajectories lead to collapse, except one which ends at the unstable steady state. This value of σ is a turning point in the bifurcation diagram shown in figure 6, and the stability of

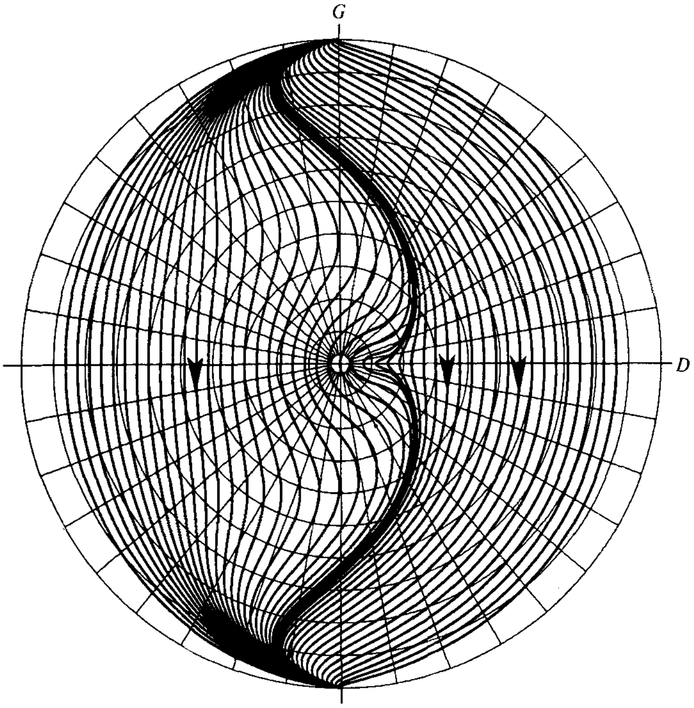

FIGURE 7. The phase plane for $\sigma = 11.0 < \sigma_{\text{cr}}$.

the solution branch changes at this point. For the full Euler equations a similar turning point exists, but it is located at a slightly larger value of σ. Saffman & Szeto (1980) claim that the stability of the steady state changes at this turning point. However, a detailed stability analysis by Dritschel (1985) shows that the change of stability occurs close to but not exactly at the turning point.

(*c*) $\sigma > \sigma_{\text{cr}}$. This is the most complicated and interesting case. We have two physically significant stationary points, and we observe from the phase portrait shown in figure 8 that there is a critical separatrix $\mathscr{S}$ starting and ending at saddle point $\mathscr{B}$. All initial conditions outside $\mathscr{S}$ lead to centroid collapse. Inside $\mathscr{S}$ we have closed orbits and the centre $\mathscr{A}$. Along a closed orbit surrounding the origin, ϕ_{d} increases steadily, so that vortices rotate counterclockwise in the corotating frame (in figure 8 where $\sigma = 12.0$ there are no orbits of this kind, but they occur for larger values of σ). However, on orbits not surrounding the origin, ϕ_{d} oscillates around zero, corresponding to a nutation of ellipses in the corotating frame. Since H has a constant value on each trajectory in the phase plane, we can characterize $\mathscr{S}$ by the value of H at the saddle point $\mathscr{B}$, namely

$$H_{\mathscr{S}}(\sigma) = \tfrac{1}{4}\pi\left[\frac{\lambda_{\mathscr{B}}^2-1}{2(\sigma\lambda_{\mathscr{B}}-\lambda_{\mathscr{B}}^2-1)} - \ln\left(\frac{\sigma\lambda_{\mathscr{B}}-\lambda_{\mathscr{B}}^2-1}{\lambda_{\mathscr{B}}}\right) - \ln\left(\frac{(1+\lambda_{\mathscr{B}})^2}{4\lambda_{\mathscr{B}}}\right) + \frac{1}{2}\right], \tag{29}$$

where $\lambda_{\mathscr{B}}$ denotes the aspect ratio of the unstable steady state $\mathscr{B}$. The region of the phase plane inside $\mathscr{S}$ is then characterized by

$$H(D, G; \sigma) < H_{\mathscr{S}}(\sigma), \quad \lambda < \lambda_{\mathscr{B}}(\sigma). \tag{30}$$

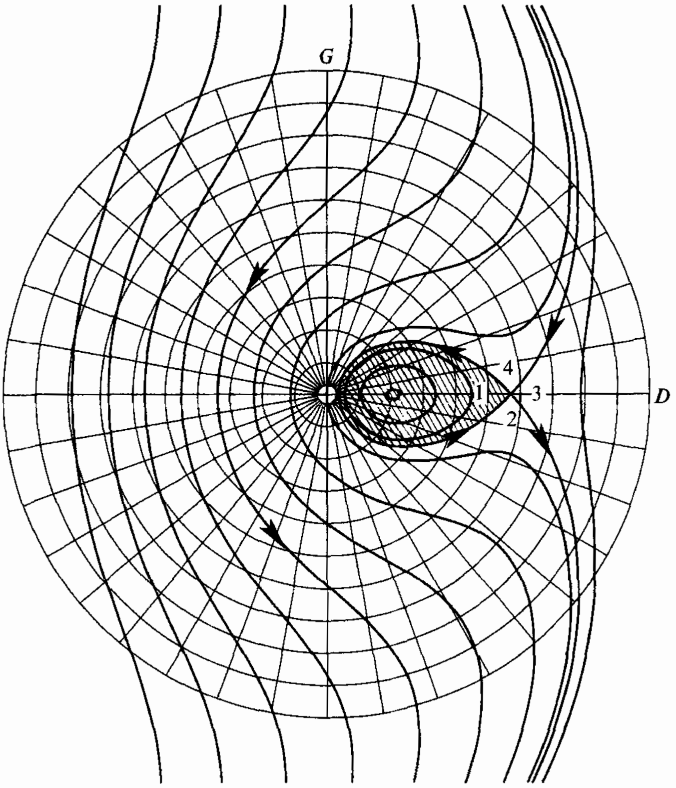

FIGURE 8. The phase plane for $\sigma = 12.0 > \sigma_{\text{cr}} \approx 11.4$. Only the central part of the diagram is shown. $\mathscr{A}$ is the centre within the hatched region and $\mathscr{B}$ is the saddle point. $\mathscr{S}$ *is the* separatrix.

Hence, *centroid collapse will occur if and only if any one of the following conditions is satisfied*:

$$\sigma < \sigma_{\text{cr}}; \quad H > H_{\mathscr{S}}(\sigma); \quad \lambda > \lambda_{\mathscr{B}}(\sigma). \tag{31}$$

Equation (31) is the first complete analytical solution of the merger problem for the Euler equations as represented by the second-order moment model. It constitutes a solution of one of the problems posed by Bassett (1888).

3.4. *An alternative view of the merger condition*

In this section we present a more easily accessible view of the merger condition (31) for the practitioner. That is, we show how the natural parameters of problem, namely the conserved quantities H and σ^{-1}, vary with the physically obvious parameters R and λ of the initial conditions. We restrict ourselves to initial conditions where the ellipses have their major or minor axis along the intercentroid axis, e.g. as shown in figure 9(*a*).

The (H, σ^{-1})-diagram of figure 9(*a*) is obtained from the definition of σ in (18) and H in (27). Curves $\mathscr{A}$ and $\mathscr{B}$ (solid and dashed, respectively) are the stable and unstable steady states discussed previously and illustrated in figure 6. Merger will occur if the initial condition is above $\mathscr{B}$ or below $\mathscr{A}$. Between $\mathscr{A}$ and $\mathscr{B}$ (e.g. at constant σ^{-1}) the system exhibits either merger or periodic solutions. The latter

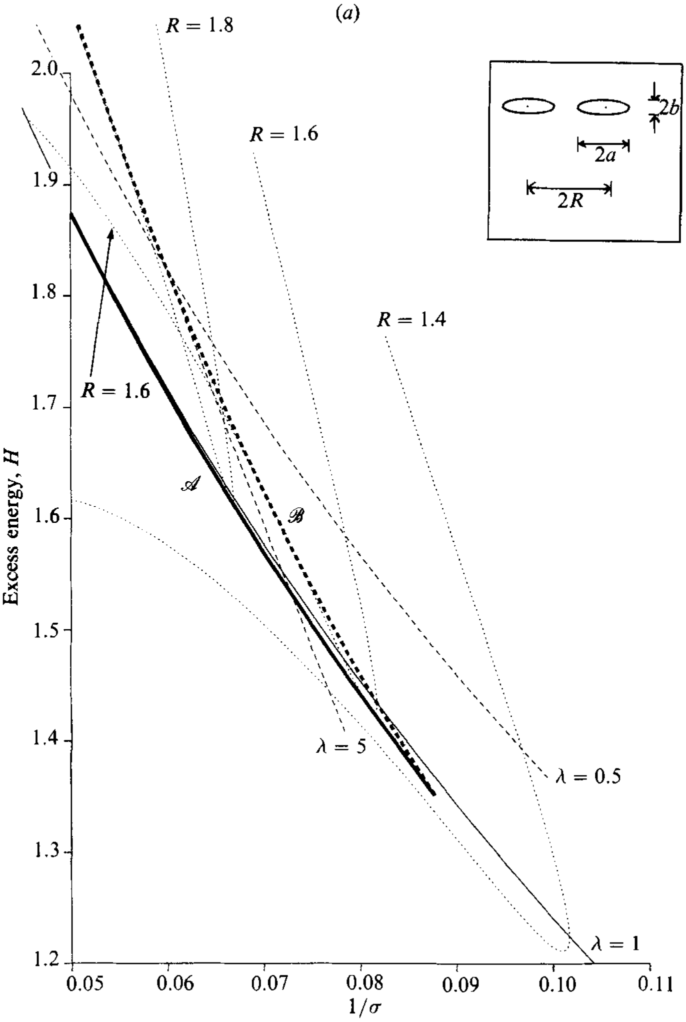

FIGURE 9(*a*). The H *vs.* σ^{-1} merger diagram for the second-order moment model with symmetric initial conditions. Curves $\mathscr{A}$ and $\mathscr{B}$ represent the stable and unstable steady states, respectively. (Also shown are curves for $R = 1.4$, 1.6 and 1.8 and $\lambda = 0.5$, 1.0 and 1.5). Merger will occur if the initial conditions are above $\mathscr{B}$ or below $\mathscr{A}$. Between $\mathscr{A}$ and $\mathscr{B}$ the system exhibits either merger or periodic solutions. The latter occurs if the λ associated with the initial conditions is smaller than $\lambda_{\mathscr{B}}$, as indicated in (31).

occurs if the λ associated with the initial condition is *smaller* than $\lambda_{\mathscr{B}}$ (as indicated in (31)). For nearly circular initial conditions, that is

$$\lambda < \min_{\sigma} \lambda_{\mathscr{B}}(\sigma) \approx 2.3,$$

the system exhibits periodic solutions between $\mathscr{A}$ and $\mathscr{B}$.

In figure 9(*a*) we show three constant-R cases (light dotted lines), $R = 1.4$, 1.6 and 1.8 and three constant-λ curves, $\lambda = 0.5$ (light dashed), 1.0 (light solid) and 5.0 (light dashed). It is clear that for $R = 1.4$ all initial conditions lead to merger. For $R = 1.6$ the curve starts in the unstable region and crosses into the stable region (near the

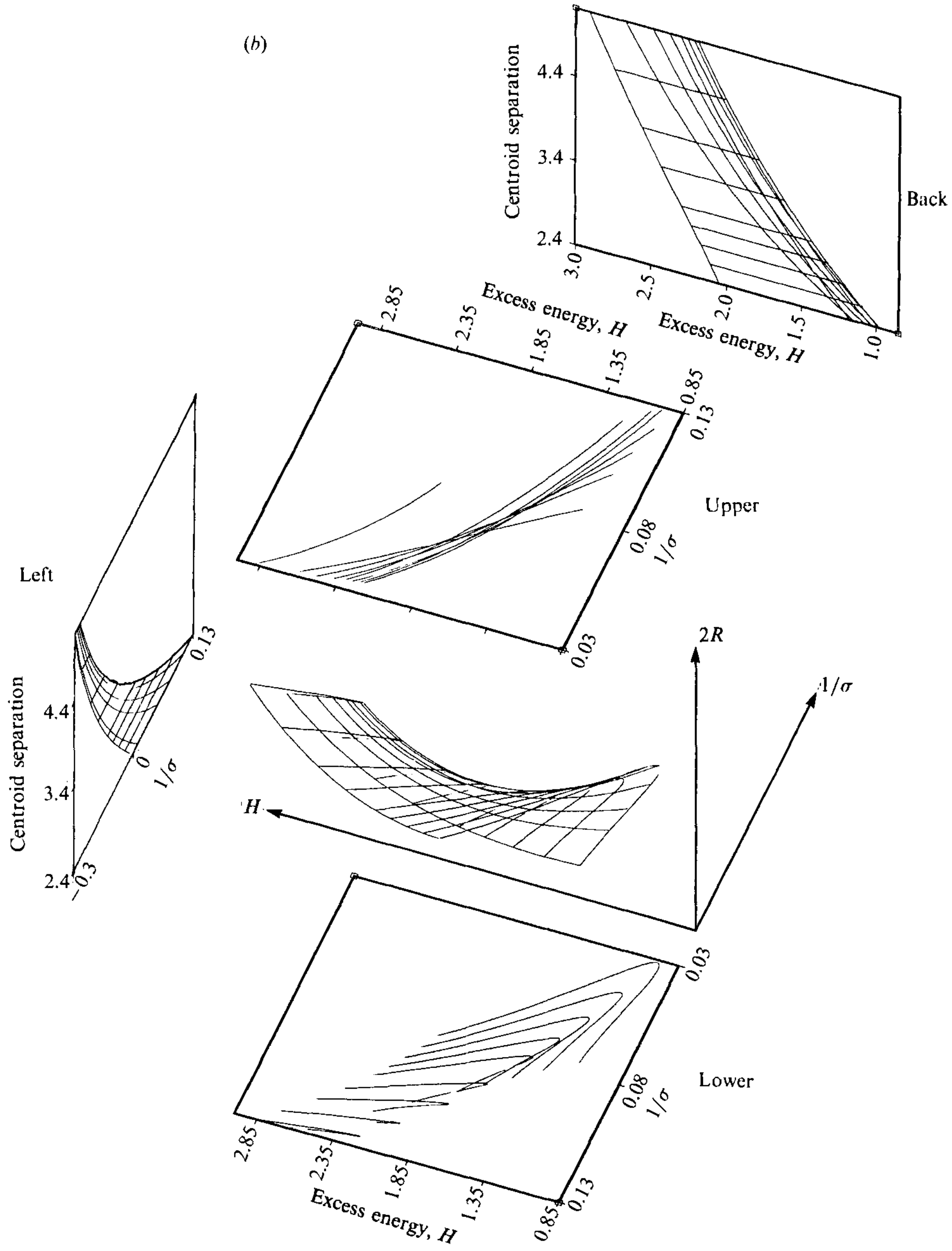

FIGURE 9(b). A three-dimensional plot of the initial states exhibited in the insert in (a). The axes are $(\sigma^{-1}, H, 2R)$. Projections of the surface on four planes are shown. The horizontal projections correspond to constant R (lower) and constant λ (upper) curves in (a). The vertical projections are included to help interpret the complex geometry of the twisting surface (hidden lines are not removed). The backplane shows $2R$ vs. H and the left-plane shows $2R$ vs. σ^{-1} and lines of constant λ are plotted.

intersection with the $\lambda = 1$ curve). It becomes tangent to curve $\mathscr{A}$ and loops upward in the stable region and becomes tangent to curve $\mathscr{B}$. At this point of tangency the stability reverses; i.e. although the $R = 1.6$ curve remains between $\mathscr{A}$ and $\mathscr{B}$ the system is unstable. Additional $R =$ constant curves (e.g. $R > 1.8$) exhibit the same qualitative behaviour. Thus we see that curves $\mathscr{A}$ and $\mathscr{B}$ arise as the envelopes of the constant-R curves.

We attempt to elucidate this complex behaviour by showing projections from the three-dimensional surface of figure 9(*b*) which defines the initial condition in the space $(\sigma^{-1}, H, 2R)$, where $2R$ is the initial intercentroid distance. The lower horizontal projection on the H *vs.* σ^{-1} diagram shows nine constant-R curves. The upper horizontal projection on the H *vs.* σ^{-1} diagram shows 8 constant-λ curves. In figure 9(*a*) we see that there are two types of constant-λ curves. For example, the $\lambda = 0.5$ and $\lambda = 1.0$ curves first intersect curve $\mathscr{B}$ as σ^{-1} decreases, whereas the $\lambda = 5.0$ curve first intersects curve $\mathscr{A}$ as σ^{-1} decreases. To assist in the interpretation of this twisting surface (note the hidden lines are not removed) we present two vertical projections, designated back and left where both constant-λ and constant-R curves are drawn.

To conclude, figure 9(*a*) not only presents a useful graphical view of the merger condition (31), but also indicates how the point-vortex model is obtained as a limit of the moment model. For example, as σ^{-1} decreases (corresponding to increasing intercentroid distance, $2R$) the $\lambda = 1$ curve intersects curve $\mathscr{B}$ and approaches curve $\mathscr{A}$ asymptotically.

4. Validation of the merger condition for the Euler equations

In this section we examine the applicability of the explicit collapse condition (31) for the Euler equations approximated by contour dynamical and weakly dissipative pseudospectral ($\nu_4 \neq 0, \nu_2 = 0$) representations. We shall plot points corresponding to an initial condition of circular vortices on the (H, σ^{-1})-diagram discussed in the previous section. We choose circular vortices to simplify the consideration and because near-circular vortex regions evolve from initially power-law energy distributions (McWilliams 1984) and elliptical vortex distributions (Melander *et al.* 1987*a*).

To locate smooth initial conditions on the (H, σ^{-1})-plane, we generalize the definition of σ:

$$\sigma \equiv 2\pi M \omega_p / \Gamma^2, \tag{32}$$

where M is the angular impulse

$$M = \iint \omega(x,y)\,(x^2+y^2)\,\mathrm{d}x\,\mathrm{d}y. \tag{33}$$

We shall now approximate M and Γ for vorticity distributions given by $V(\delta, \omega_p, a, b)$. We consider two vortex regions situated symmetrically around the common vorticity centroid. The distance between the individual centroids we designate $2R$. Furthermore let $A(\zeta)$ be the area of the vorticity contour $\omega = \zeta$ of one vortex. Thereby, we have

$$M = 2\Gamma R^2 + \frac{1+\lambda^2}{2\pi\lambda} \int_0^{\omega_p} A^2(\zeta)\,\mathrm{d}\zeta, \tag{34}$$

or

$$M \approx 2\Gamma R^2 + \frac{(1+\lambda^2)\,\pi\omega_p b^4}{(5120)\,\delta\lambda}\left[(4-\delta)^5-(4-3\delta)^5\right], \tag{35}$$

Evolution	Algorithm	δ	$\frac{1}{\sigma}$	H
P	S	1.00	0.05120	1.937
P	S	1.00	0.05123	1.936
P	S	1.00	0.05494	1.907
M	S	1.00	0.05765	1.879
M	S	1.00	0.06055	1.846
M	S	1.00	0.06531	1.787
M	S	1.00	0.09187	1.457
P	S	0.75	0.06314	1.736
P	S	0.75	0.06504	1.710
P	S	0.75	0.06702	1.683
P	S	0.50	0.05252	1.846
P	S	0.50	0.06891	1.614
PE	S	0.50	0.07261	1.565
M	S	0.50	0.07289	1.562
M	S	0.50	0.07717	1.509
M	S	0.50	0.09842	1.276
P	CD	0.00	0.06476	1.646
P	CD	0.00	0.07352	1.520
PE	CD	0.00	0.07376	1.518
M	CD	0.00	0.10979	1.147

TABLE 1. The first column gives the result of the long-time evolution, M = merger, P = pulsation, PE = pulsation with exchange of vorticity. The second column gives the numerical algorithm used, S = spectral code, CD = contour dynamics. σ is the dimensionless angular impulse and H is the dimensionless excess energy.

where we have approximated $V(\delta, \omega_p, a, b)$ by an elliptical frustrum of a cone, see Melander *et al.* (1987*a*). Using the same approximation we find

$$\Gamma = \int_0^{\omega_p} A(\zeta)\,\mathrm{d}\zeta \approx \omega_p \pi a b(1-\delta+13\delta^2/48). \tag{36}$$

The excess energy $-\frac{1}{2}\int \omega\psi\,\mathrm{d}x\,\mathrm{d}y$ is determined only up to an arbitrary additive constant because the stream function is determined only up to an arbitrary additive constant. Thus when we compare two different methods it is of importance to use exactly the same stream function. Owing to the logarithm in (36) we have to choose a characteristic lengthscale L before we can fix the additive constant. A natural normalization of ψ arises when its large-r expansion has no constant term,

$$\psi(x,y) = -\frac{1}{4\pi}\iint \omega(\xi,\eta)\ln\left[\frac{((x-\xi)^2+(y-\eta)^2)}{L^2}\right]\mathrm{d}\xi\,\mathrm{d}\eta. \tag{37}$$

The stream function used in the moment model obeys this normalization with $L = (A/\pi)^{\frac{1}{2}} = (\Gamma/\omega_p\pi)^{\frac{1}{2}}$. Our simulations with smooth vorticity distributions are done with a pseudospectral numerical code (Haidvogel 1985) in the domain $[-\pi,\pi]\times[-\pi,\pi]$. Both ω and ψ are normalized such that their area integrals over the box vanish. Although these normalizations do not affect the velocity field, they obviously affect the excess energy. In order to ensure the same normalization as for the moment model, we calculate H and ψ using only the initial condition and (37). Thus, we neglect the influence of the periodic boundary conditions and dissipation. (Another

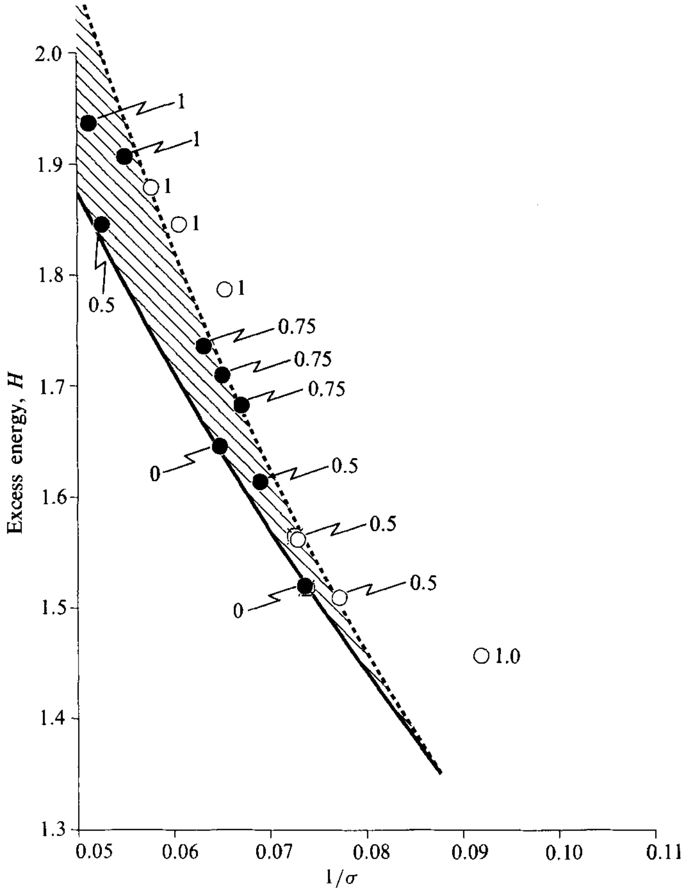

FIGURE 10. For moderate aspect ratios ($\lambda < 2.3$) the merger condition reduces to a relation between H and σ. In the (σ^{-1}, H)-plane the corotating steady states form two curves. The upper curve (——) represents the stable steady states; the saddle points in the phase plane are located on the lower curve (– – – –). The shaded region between the two curves represents all the pulsating solutions. Results from continuum model simulations (table 1) are also plotted in the diagram: (○) merging solutions, (●) pulsating solutions. The number at each circle gives the value of $\delta = (R_o - R_i)/R_o$, and shows the insensitivity of the collapse condition to δ.

detailed discussion of the excess energy and an efficient way of calculating it in contour-dynamical simulations is given in Dritschel (1985).)

Table 1 presents a list of continuum model simulations which are also plotted on figure 10. For each simulation the value of H and σ^{-1} is shown, together with the result of the long-time evolutions, that is, merger or pulsation. We observe a remarkable agreement, that is, the open circles (done with $\lambda = 1$) which correspond to merger are in the outer region where the moment model indicates collapse. The numbers adjacent to the circles in figure 10 show the values of δ in $V(\delta, \omega_p, a, b)$. Although the moment model does not contain the parameter δ we see that the collapse condition is insensitive to the vorticity profile as given by δ. Increasing δ (namely, values of 0.5, 0.75 and 1) displaces the $\lambda = 1$ curve downward on the (H, σ^{-1})-diagram but does not affect the stability–instability transition.

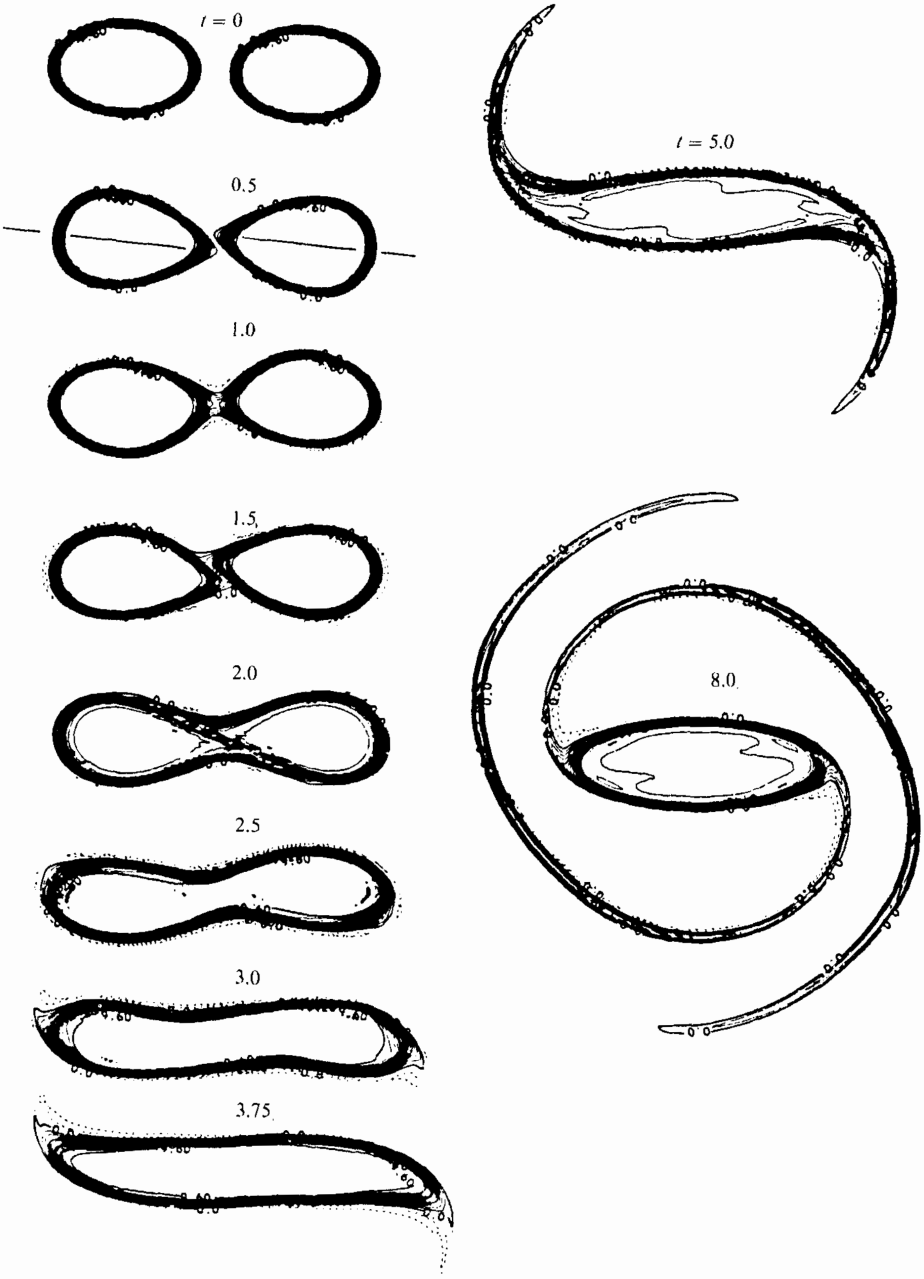

FIGURE 11 (Part 1). For caption see facing page.

5. Verification of the model's dynamical prediction

The moment model not only provides us with an explicit merger condition (31), but uncovers some interesting dynamical features of the merger phenomenon – particularly, that the presence of an unstable steady state is crucial for the merger process. At this steady state (the saddle point $\mathscr{B}$ in the plane, figure 8) the trajectories leading to merger are separated from the trajectories not leading to merger by the critical separatrix $\mathscr{S}$. We shall now make a reasonable demonstration that there is

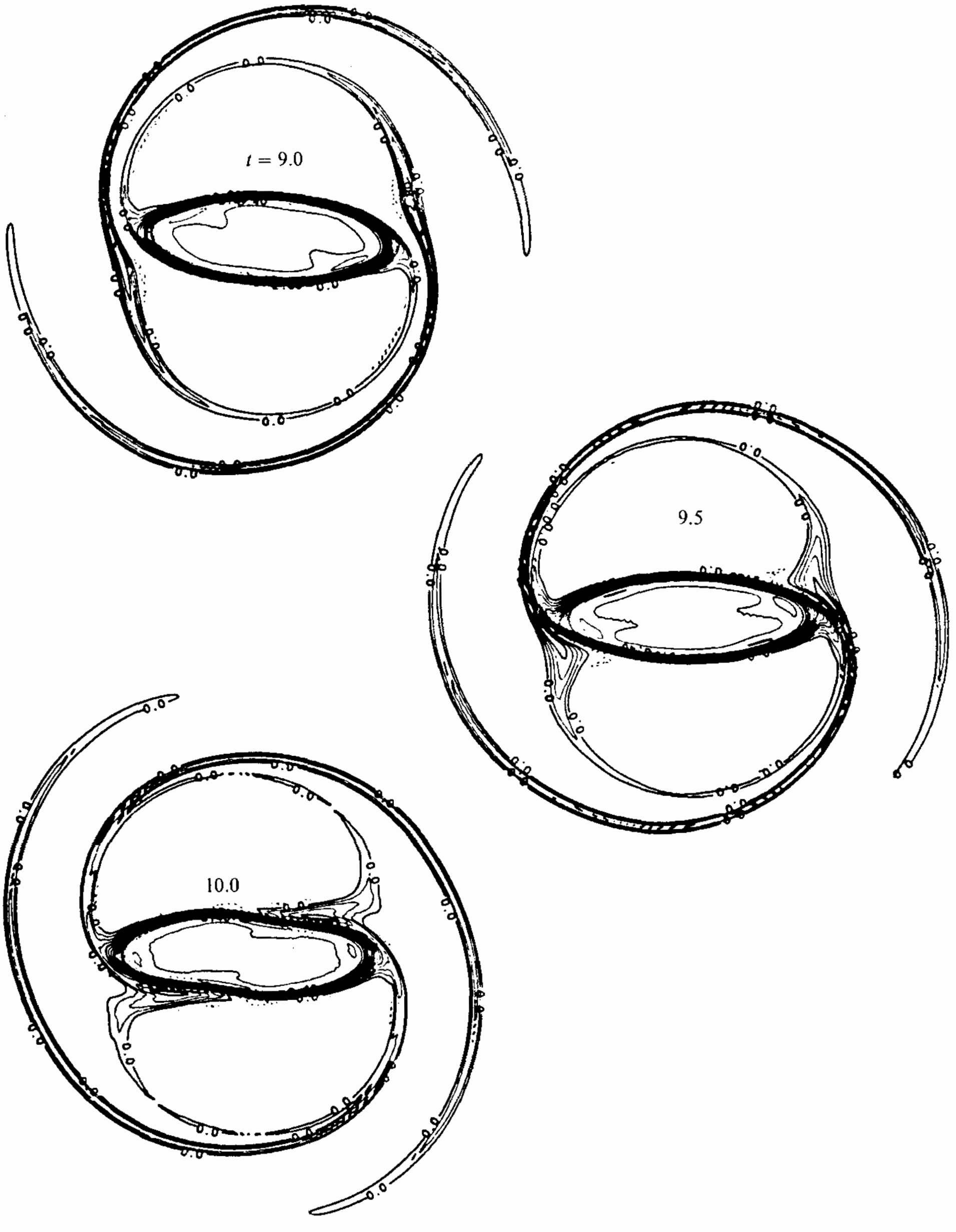

FIGURE 11. Evolution of the vorticity for two symmetrically placed states $V(0.2, 10.0, 0.6255, 0.4)$ on a 256^2 mesh with $\nu_4 = 3.125 \times 10^{-8}$. The initial intercentroid distance is 1.44 and the box size is 2π. We have subtracted the bulk rotation in the picture since it is irrelevant for our discussion. The contour interval is 0.6.

a corresponding unstable state in the full Euler equations at the threshold to merger. We do that by the use of two high-resolution simulations – corresponding to initial conditions on either side of the critical separatrix $\mathscr{S}$.

Figure 11 shows a numerical simulation of the evolution of two isolated vortex regions in a corotating frame as calculated on a 256^2 mesh with $\nu_4 = 3.125 \times 10^{-8}$. The initial conditions, chosen to correspond to the Overman & Zabusky (1982) simulations, are near top hat (small δ) of elliptical shape, $V(0.2, 100, 0.6255, 0.4)$, and have $\sigma = 12.66$. By trial and error we have adjusted the centroid separation to 1.44, which is slightly smaller than the critical merger separation. We observe that the two vortices approach and the lower contours reconnect at $t = 1.0$. As the vortices continue to approach each other, steep vorticity gradients form along an almost straight-line interface between the vortices, where the dissipation acts strongly and the interfacial contours are erased. The excess vorticity, defined to be the vorticity outside the core radius C_1 and C_2 shown in figure 2(*a*), is initially confined to the $\mathscr{E}$-band and is convected around both core regions. In fact, the excess vorticity is due to the non-ellipticity of these regions. Therefore, we observe the arrival of two separated regions of excess vorticity at the central stagnation point A_3 at $t = 0.5$ and at $t = 1.5$. A careful study of the pictures, showing the evolution until $t = 3.75$, enables us to follow the transport of excess vorticity in the $\mathscr{E}$-band. For example, at $t = 2.5$ a region of excess vorticity arrives at the stagnation point A_1 and a similar region arrives at A_2. In the meantime, the location of the stagnation point has changed slightly, such that part of the excess vorticity is *outside* the $\mathscr{E}$-band and filamentation begins at $t = 3.0$. From this point on the evolution is an axisymmetrization of a single vortex core, as described in Melander *et al.* (1987*a*).

We observe that the state barely changes its shape in the time interval from $1.0 \leqslant t \leqslant 3.0$. During this period the state looks like an unstable steady state ($\mathscr{B}$) predicted by the moment model. After $t = 2.5$ we can no longer distinguish the individual vortices, since the dissipation has erased the gradient between them. For $t > 3.0$ the compound core begins to axisymmetrize. We display pictures of this evolution because they constitute a unique example of the evolution after a merger of nearly uniform vortices (comparable to contour dynamics) and because they highlight the complicated entanglement of long filaments. At $t = 5.0$ we see a significant vorticity shedding and the formation of strong filaments. The almost complete absence of the 'roll-up' phenomenon is due to the smooth vorticity distribution which increases the 'roll-up' timescale (Pullin & Phillips 1981) but has nothing to do with the periodic boundary conditions (actually the periodic boundary conditions are in favour of the roll-up). At $t = 8.0$ the vorticity shedding has stopped and a near-elliptical core has formed. The presence of the filaments has a dramatic influence on the core, particularly when they reattach to the core. The figures at $t = 9.0$, $t = 9.5$ and $t = 10.0$ represent our cleanest example of a reattachment. The evolution beyond $t = 10.0$ has not been calculated, but is within the framework of the axisymmetrization of a single vortex (Melander *et al.* 1987*a*). We expect relaxation to axisymmetry through further 'breakings', that is, ejections of vorticity from the core. Note that at early times D. G. Dritschel (1987, private communication), using the contour-dynamics surgery code, has observed similar results, including reattachment.

While figure 11 corresponds to a trajectory slightly outside the critical separatrix $\mathscr{S}$ in the phase plane, figure 12 corresponds to a trajectory slightly inside $\mathscr{S}$. This figure is the result of a 128^2 mesh calculation with $\nu_4 = 50 \times 10^{-8}$. We begin with the same initial conditions as previously, but the centroid separation is now increased to 1.45. Except for the obvious smoothing effect of increased dissipation, the evolution until $t = 2.0$ is the same as before. In the time interval from $t = 2.0$ to $t = 5.0$, we observe an almost steady state corresponding to the saddle point in the phase plane. At $t = 7.0$ this state begins to break into two vortices and at $t = 8.5$ only the two lowest contours are joined. The vortices approach again at $t = 9.0$ and at $t = 10.0$ we observe a near recurrence to the steady state. Note that these two vortices will merge eventually owing to the presence of dissipation, which slowly reduces the magnitude of σ to a value below σ_{cr}, as will be discussed in §6.

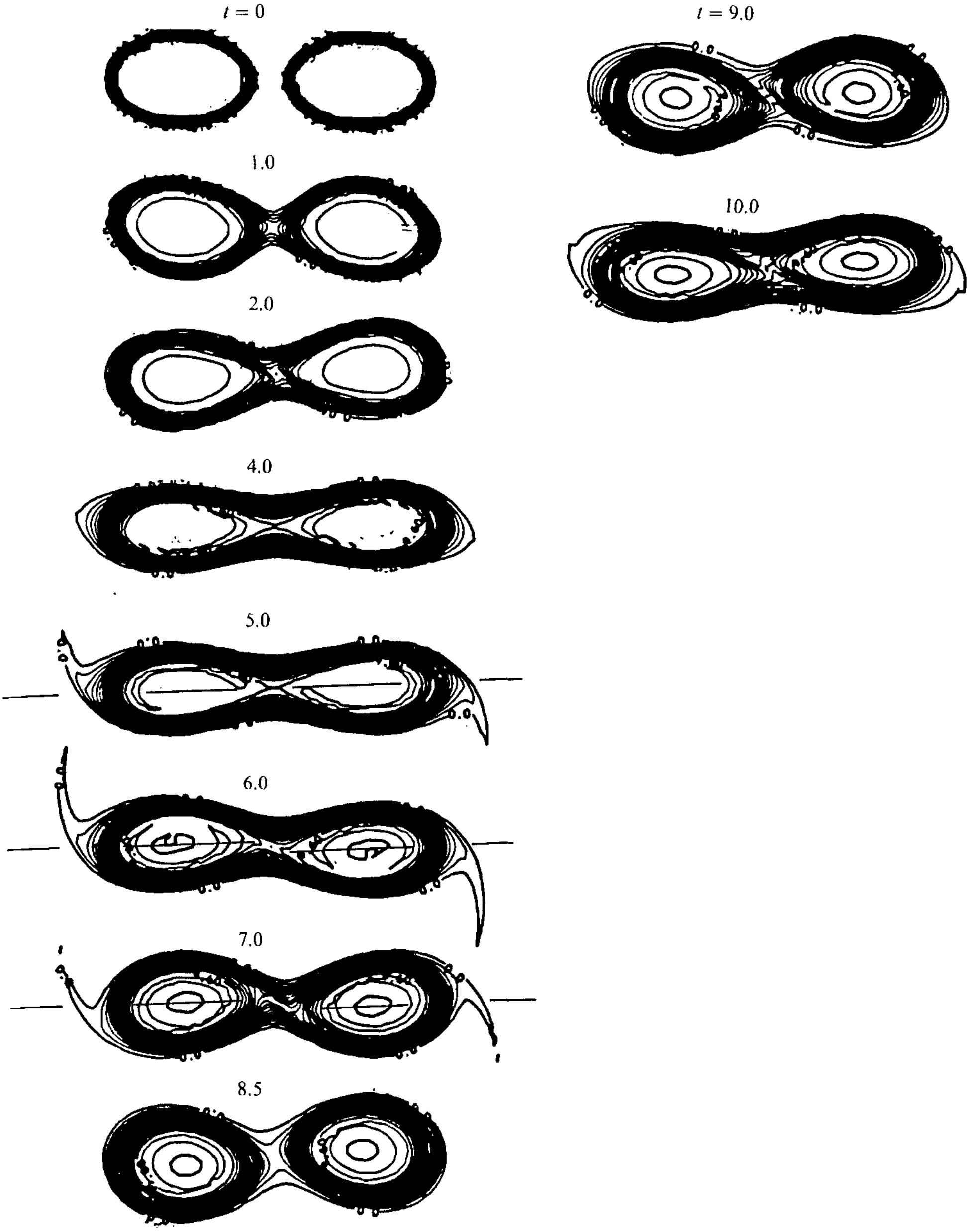

FIGURE 12. Evolution of the same two vortices as in figure 11 but with the initial intercentroid separation increased to 1.45. The calculation is performed on a 128^2 mesh with $\nu_4 = 50 \times 10^{-8}$.

In the case that $\sigma > \sigma_{cr}$ the moment model yields simple rules of thumb for determining if merger is going to occur. Table 2 presents simple rules for determining long time evolution from a short-time evolution in the vicinity of the saddle point $\mathscr{B}$. The separatrices divide this region of the phase plane into four sectors, labelled in figure 8. For initial conditions near the threshold to merger the trajectory will enter one of these sectors in less than half a revolution in the corotating frame. That is, one sees the long-time evolution from about half a revolution in the corotating frame.

It is easy to recognize a vorticity configuration corresponding to a state in the neighbourhood of the saddle point $\mathscr{B}$ because the vortices are aligned and fairly

Sector (see figure 8)	Characteristic	Long-time evolution
1	$\dot{\phi}_{\mathrm{d}} > 0$	Periodic pulsation (non-merger)
2	$\ddot{\phi}_{\mathrm{d}} < 0, \dot{\phi}_{\mathrm{d}} \approx 0$	Merger
3	$\dot{\phi}_{\mathrm{d}} < 0$	Merger
4	$\ddot{\phi}_{\mathrm{d}} > 0, \dot{\phi}_{\mathrm{d}} \approx 0$	Merger after one pulsation

TABLE 2. Correspondence of short-time and long-time evolutions according to initial locations in the (D, G)-phase plane.

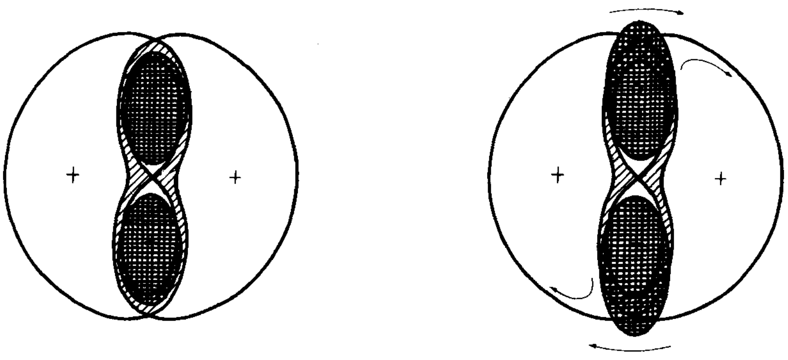
sector (1) sector (3)

sector (2) sector (4)

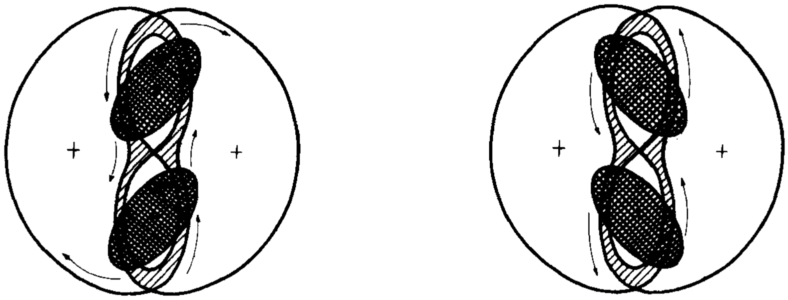

FIGURE 13. Four different perturbations of the unstable corotating steady state (B). Each perturbation corresponds to a point in one of the four sectors around the saddle point in the phase plane (figure 8).

elongated, $\lambda > \min_{\sigma}\{\lambda_{\mathscr{B}}\} \approx 2.36$. Furthermore, the points on the D-axis between $\mathscr{A}$ and $\mathscr{B}$ are characterized by: $\dot{\phi}_{\mathrm{d}} = 0$; $\ddot{\phi}_{\mathrm{d}} > 0, \dot{\lambda} = 0$; $\ddot{\lambda} < 0$, where the last follows from (26) since (D^2+G^2) is a maximum and therefore λ is a maximum.

Table 2 shows that merger occurs if $\dot{\phi}_{\mathrm{d}}$ along the trajectory is or becomes negative in the neighbourhood of the saddle point $\mathscr{B}$. From (21) we observe that $\dot{\phi}_{\mathrm{d}}$ becomes negative only when the clockwise rotation caused by the mutual interaction dominates the counterclockwise rotation of the Kirchhoff ellipse. At the stationary points $\mathscr{A}$ and $\mathscr{B}, \Omega_{\mathrm{m}} = \Omega_{\mathrm{s}}$. Hence, we conclude that merger will occur if and only if the balance at the saddle point $\mathscr{B}$ between self- and mutual-interaction is changed such that $\Omega_{\mathrm{m}} > \Omega_{\mathrm{s}}$.

We observe that these rules apply to the simulations in figures 11 and 12. In figure 11 we observe from $t = 1.0$ to $t = 2.5$ a slow clockwise rotation of the individual vortices with respect to a corotating frame. Thus, according to table 2 the long-time evolution leads to merger. In figure 12 the vortices rotate counterclockwise as seen by comparing $t = 5.0$, $t = 6.0$ and $t = 7.0$. Thus, the long-time evolution does not lead to merger.

We now have two views of the symmetric merger. One, presented in §2, is a physical space – kinematic view, which highlights the importance of the vorticity distribution relative to the stagnation points of the corotating stream function ψ_c. The other view is a phase-space representation introduced by the moment model.

We now juxtapose these points of view and compare evolutions subject to small perturbations in the vorticity field of the unstable state $\mathscr{B}$. Since the location of the separatrices of ψ_c is insensitive to small perturbations of the vorticity field, we assume ψ_c is unchanged in the four panels of figure 13. A point in sector 2 is obtained by tilting the vortices slightly clockwise. Thereby, particles carrying vorticity can be trapped in the ghost vortices as indicated in figure 13. These particles will be convected into filaments along the outer separatrices o_1 and o_2, thereby causing the vorticity field to become more axisymmetric, as discussed in Melander *et al.* (1987*a*). A point in sector 4 is obtained by tilting the vortices clockwise. Again, vorticity gets trapped in the ghost vortices as shown in figure 13 but is not convected immediately into the filaments. However, after half a rotation in the corotating frame we obtain a configuration similar to figure 13. A point in sector 3 is obtained by elongating the vortices and decreasing slightly the centroid separation subject to the constraint that the moment of inertia is conserved. Thus, as shown in figure 12, vorticity is displaced outside the $\mathscr{E}$-band, which will result in filamentation and axisymmetrization. A point in sector 1 is obtained by making the vortices more circular and increasing the centroid separation slightly. This perturbation causes the vorticity to be redistributed in the $\mathscr{E}$-band, as shown in figure 13. Hence, we expect a pulsating state with exchange of vorticity between the vortices, as in figure 12.

6. Dissipation and the approach towards a metastable state

In this section we examine the role of dissipation on the formation of long-lived metastable states and merger. We generalize the moment model to include a primitive model of the Newtonian viscosity. The derivation is given in Appendix B. (Note, it is not possible to include the hyperviscosity, without including fourth-order moments.)

Each vortex region is modelled as an ellipse of area $A(t)$ and uniform vorticity $\omega(t)$ such that the circulation Γ is constant, and we introduce a dimensionless viscosity $\nu \equiv \nu_2/\Gamma$. Hence the evolution of each vortex region is described by five variables, namely, the centroid position (x_k, y_k), the aspect ratio λ_k, the orientation ϕ_k and the area A_k. For a symmetric initial condition we suppress subscripts, and the aspect ratio λ and area A evolve according to

$$\dot{\lambda} = 4\pi\frac{\nu}{A}(1-\lambda^2)+\lambda\frac{\Gamma}{4\pi R^2}\sin 2(\theta-\phi) \tag{38}$$

and

$$\dot{A} = 4\pi\nu(1+\lambda^2)/\lambda, \tag{39}$$

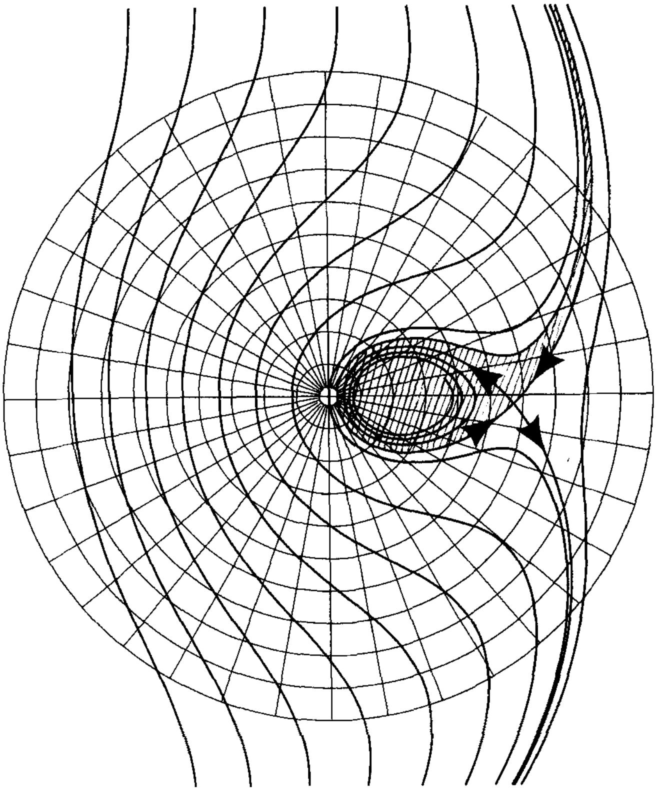

FIGURE 14. The 'adiabatic' phase plane $\sigma(0) = 12.0, \nu = 10^{-3}$. The central part corresponding to figure 8 is shown. The points in the shaded region do not lead to merger on the convective timescale.

while the remaining evolution equations (15), (16) and (17) are unchanged. Note that the new leading term of (38) drives λ toward unity and (39) shows that A increases. The rate of change of the total angular impulse M is identical to the Poincaré identity for the Navier–Stokes equations

$$\dot{M} = 4\nu\Gamma. \tag{40}$$

Therefore, we can reduce the number of equations and variables in the case of two identical vortices to three non-autonomous differential equations in the variables D, G and A:

$$\begin{pmatrix}\dot{D}\\ \dot{G}\end{pmatrix} = -\frac{4\pi\nu}{A}[(4+D^2+G^2)(D^2+G^2)]^{\frac{1}{2}}\begin{pmatrix}D\\ G\end{pmatrix} + \left[K(2+KD)-\frac{2}{2+(4+D^2+G^2)^{\frac{1}{2}}}\right]\begin{pmatrix}G\\ -D\end{pmatrix}-\begin{pmatrix}0\\ K(4+D^2+G^2)^{\frac{1}{2}}\end{pmatrix}, \tag{41}$$

$$\dot{A} = 4\pi\nu(4+D^2+G^2)^{\frac{1}{2}}. \tag{42}$$

Here we have introduced a non-dimensional time, measured in units of $1/\omega(0)$. Furthermore, $\sigma = 2\pi M/\Gamma A$ is now a function of time.

When $\nu \ll 1$ the problem has two characteristic timescales, a convection timescale (t) and a dissipation timescale (νt). Since σ and A change only on the slow timescale,

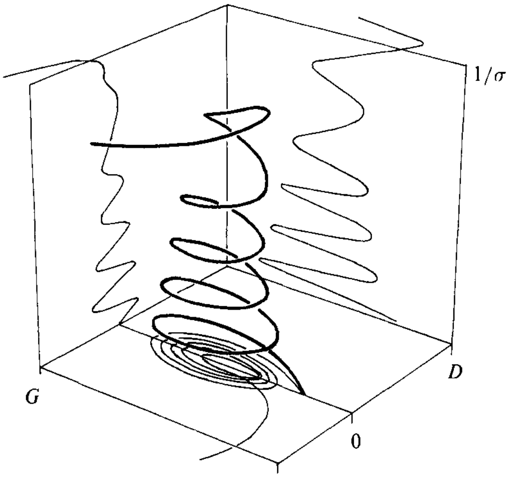

FIGURE 15. The actual behaviour of the evolution in the (D, G, σ^{-1})-space for the dissipative model with $\sigma(0) = 12.0$ and $\nu = 10^{-3}$.

we can ignore the time dependence of these quantities for the study of short-time evolutions. Thus, for $|t-t_0| \ll 1/\nu$ we replace $\sigma, A(t)$ in (41) by $\sigma(t_0), A(t_0)$. Thereby, (42) decouples from (41) and the equations become autonomous. This allows us to introduce the 'adiabatic' phase plane shown in figure 14 for $\sigma(0) = 12.0$.

We observe that $\mathscr{A}$ has changed to an attracting fixed point and the separatrix $\mathscr{S}$ now extends to the circle C_0, where $R = 0$. Thereby, there exist *new* initial conditions (hatched area) that do *not* lead to centroid collapse on a circulation timescale. Trajectories through these points spiral inwards towards the stable fixed point $\mathscr{A}$. Furthermore, the steady states are no longer located exactly on the positive D-axis, but slightly below it.

For long-time evolutions, the time variation of σ and A results in a slow change of the adiabatic phase plane. Since $\dot{\sigma}$ is negative and never approaches zero the two fixed points will eventually disappear, causing a convective merger. Figure 15 shows a simulation in the $(D, G, 1/\sigma)$-space with the dissipative moment model. We see D and G undergoing near periodic oscillations until σ decreases below a critical value approximately equal σ_{cr}, when a centroid collapse occurs.

The dissipative moment model has a 'metastable' state, namely, the stable fixed point $\mathscr{A}$ in the adiabatic phase plane. This state changes slowly in time, that is, λ and A increase slowly, while $\phi_{\mathrm{d}} = \phi - \theta$ remains almost zero. The metastable state has a finite lifetime, namely, the time it takes for σ to decrease to σ_{cr} and the state subsequently disappears in a convective merger.

In order to compare the dissipative moment model with pseudospectral simulations we must have a relatively strong dissipation, say $\nu_2 = \nu\Gamma = 10^{-3}$. This follows because we wish to observe the slow approach towards the metastable state and its slowly increasing aspect ratio without excessive use of computer time. For numerical reasons, the mesh size is linked to the magnitude of the smallest dissipation in the spectral code. A Newtonian dissipation $\nu_2 = 1.52 \times 10^{-3}$ is used for a 64^2 mesh. In order to obtain a well-resolved vorticity distribution on this mesh we choose the initial conditions of two $V(1, 20, 0.8, 0.8)$ vortices. Their initial centroid separation was chosen to be slightly larger than the non-dissipative critical merger separation, namely $x_1 - x_2 = 1.7136$.

The simulation shown in figure 16 shows three full revolutions of the vortices

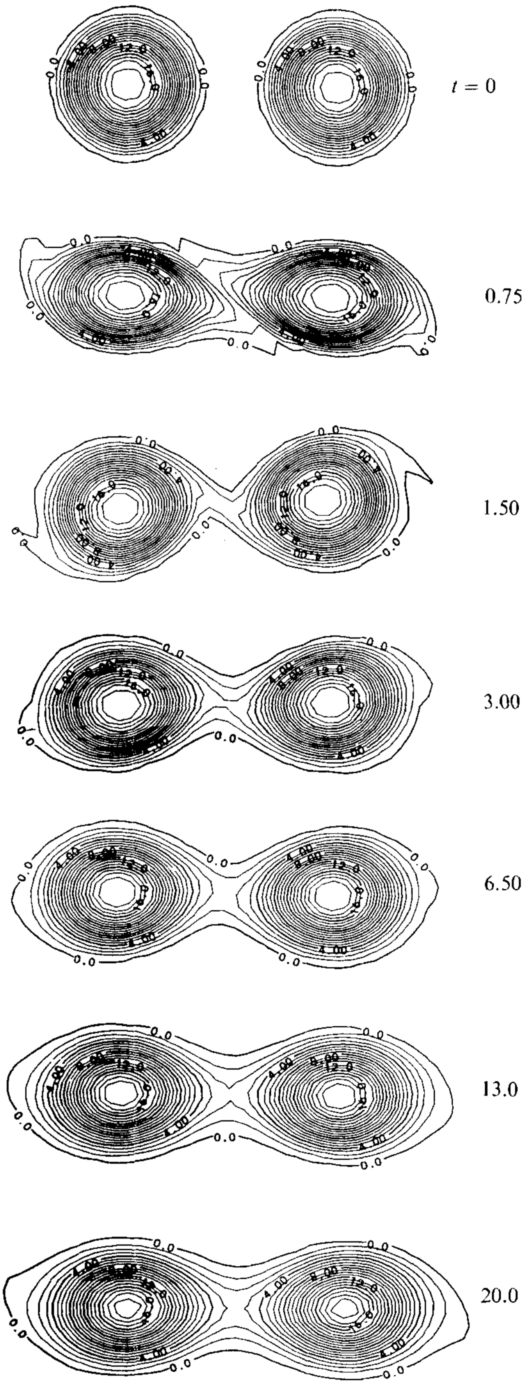

FIGURE 16. The evolution of two $V(1.20, 0.8, 0.8)$ vortices with an initial centroid separation of 1.7136. The calculation is done on 64^2 mesh with $\nu_2 = 1.52 \times 10^{-3}$.

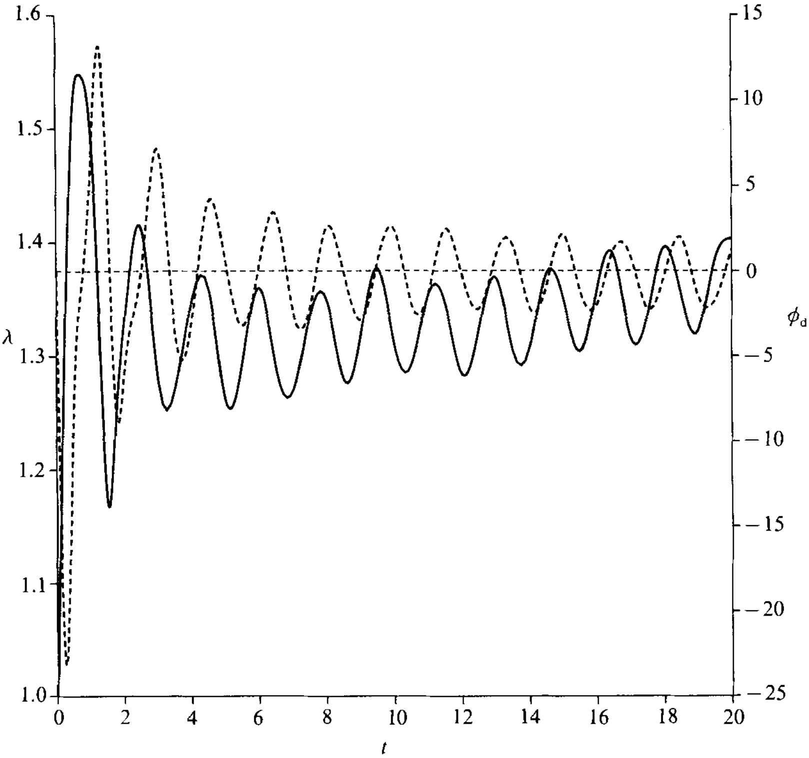

FIGURE 17. Diagnostics for the evolution shown in figure 16. For one of the contours at vorticity level $\omega = 8.0$ we have calculated the aspect ratio λ (——) and the orientation in the corotating frame ϕ_d (---).

around their common vorticity centroid in a corotating reference frame. We observe an approach towards a metastable state. After the first revolution, $t \approx 6.5$, the vorticity configuration remains almost unchanged throughout the rest of the simulation. We can explain this slowly changing configuration using the dissipative moment model. However, the initial transient during which the metastable state forms, $0 \leqslant t \leqslant 6.5$, is not described by the model, as discussed below.

We have calculated the aspect ratio and the orientation ϕ_d in a corotating frame of the contour $\omega = 8.0$, as shown in figure 17. The aspect ratio λ of this contour oscillates around a steadily increasing average value and ϕ_d oscillates around zero, corresponding to a nutation in the corotating frame. Similarly, in the moment model, λ and ϕ_d behave in the same way along a trajectory that spins around the stable fixed point in the adiabatic phase plane. Furthermore, the slowly increasing average aspect ratio of the $\omega = 8.0$ contour is similar to the slowly growing aspect ratio of the metastable state in the moment model. The slowly increasing average aspect ratio of the individual vortices, evident in figures 16 and 17, is somewhat counterintuitive. Intuitively, one would have expected that individual vortices become increasingly circular in the presence of dissipation. However, the dissipative moment model explains satisfactorily why that does not happen.

Note, when the vorticity configuration corresponds to a point (D, G) in the neighbourhood of the saddle point, e.g. in the phase plane in figure 16 at $t \approx 0.75$, steep gradients develop along an interface between the two vortices and are strongly affected by dissipation. This enhances the rate of approach to the metastable state.

The moment model does not contain this strong dissipation near the saddle point. Hence, one possible way of modelling this phenomenon would be to include a nonlinear dissipation $\nu(D, G)$.

7. Conclusion

This paper takes the first step towards an analytical understanding of the merger of two isolated like-signed vortex regions. For reasons of mathematical simplicity we have considered the merger of a symmetric vortex system.

We apply a complementary modelling approach and use three algorithmic representations of the Euler and Navier–Stokes equations. For high-resolution continuum distributions of vorticity we make simulations with a pseudospectral code. For piecewise-constant distribution of vorticity we refer to contour-dynamical results, in the literature. Finally, for a low-order analytically tractable model of the Euler equations we use the Hamiltonian moment model. This model is simple yet involves sufficient degrees of freedom to capture the first stages of a merger. By juxtaposing results obtained from these very different models, we arrive at the conclusions listed below.

The long-time result of an isolated merger process is an axisymmetric monopole surrounded by a tangle of nearly concentric filaments. The chief mechanism in the evolution towards axisymmetry is filament generation. The details are described in Melander *et al.* (1987*a*), where we investigate the axisymmetrization of an isolated elongated vortex. The similarities and small differences between these two processes are highlighted in §2.

The dimensionless angular impulse σ, defined in (18) or (32), is an essential parameter in the merger problem. The existence of steady corotating states depends on the value of σ. There is a critical vaue of σ below which no steady corotating states exist. Above $\sigma_{\mathrm{cr}} \approx 11.4$ stable and unstable states coexist. The steady corotating states are of paramount importance. If no such states exist (i.e. $\sigma < \sigma_{\mathrm{cr}}$) all initial conditions lead to merger, whereas if steady corotating states exist some initial conditions lead to merger while others do not. We remark that σ_{cr} may depend on the vorticity amplitude distribution. In the following we shall consider initial conditions with a fixed vorticity amplitude distribution.

For $\sigma > \sigma_{\mathrm{cr}}$ there exists at least one unstable steady corotating state. For the moment model there is exactly one such state and it is located exactly on the merger threshold. That is, we can find both merging and pulsating solutions that at some point in time get arbitrarily close to the unstable steady state. In fact, a continuous change from a merger initial condition to a pulsation initial condition will pass through an initial condition from which the dynamical evolution asymptotically approaches the unstable steady state. We have performed this procedure with the moment model, figure 4, and with the pseudospectral algorithm, figures 11 and 12. Also, Zabusky *et al.* 1979, performed this procedure using contour dynamics. However, the simulations were not carried far enough in time to reveal the unstable steady state and its crucial importance.

The importance of the unstable steady state is clear from the merger condition (31) which is derived from the integrable Hamiltonian moment model. The critical constants in the merger condition are derived directly from the unstable steady state. The merger condition, which is the single most important contribution in this paper, allows us to determine from a given initial condition if merger will occur or not – at least for the moment model. We expect a generalization of the merger condition for the full Euler equations to be close to (31). In order to justify this point of view we have compared the moment-model merger condition (31) with results from pseudospectral simulations. The agreement is striking (figure 10), but not exact.

When a weak Newtonian viscosity is included in the model, the symmetric merger problem leads to three ordinary differential equations which obey the Poincaré identity, $\dot{M} = 4\Gamma\nu$. All initial conditions eventually lead to merger! For some, this occurs in a circulation timescale, whereas the others are attracted to a metastable state which has a lifetime governed by the dissipation timescale. This metastable state disappears eventually in a convective merger. The existence and slow evolution of this state are well explained by the dissipative moment model. For initial conditions close to the inviscid merger threshold, the attraction towards the metastable state is stronger in the Navier–Stokes equations than in the dissipative moment model.

In nature the ideal conditions that we have considered in this paper are rare. Nonsymmetric vortices interact in the presence of strain fields produced by remote vortices (e.g. shear layers and wakes), possibly in the vicinity of boundaries, and local topography variations. Stratification and weak three-dimensional effects can be important at intermediate and long times, at which time the dissipation becomes important. However, we believe that the physical processes and conditions we have identified are of the essence. That is, they will provide a robust basis for considering the various parameters introduced by the physical processes enumerated above.

The work of N. J. Zabusky and M. V. Melander was supported by the US Army Research Office, Contract DAAG 29-84-K-0149 and the Office of Naval Research, Contract N00014-85-K-0029. The work of J. C. McWilliams was supported by the National Science Foundation. The simulations were done on the CRAY-1 at the National Center for Atmospheric Research which is supported by the National Science Foundation.

Appendix A. Energy and enstrophy decay rates

We obtain decay rates for the evolution of energy and enstrophy from (1) and (2) and the definition of excess energy

$$E = -\frac{1}{2}\int_{R^2} \psi\omega \,\mathrm{d}\sigma$$

and the enstrophy

$$Z = \int_{R^2} \omega^2 \,\mathrm{d}\sigma.$$

For the change of energy we have

$$\begin{aligned}\dot{E} &= -\frac{1}{2}\frac{\mathrm{d}}{\mathrm{d}t}\int_{R^2} \omega\psi \,\mathrm{d}\sigma = -\frac{1}{2}\frac{\mathrm{d}}{\mathrm{d}t}\int_{R^2} |\nabla\psi|^2 \,\mathrm{d}\sigma = -\int_{R^2} \psi\frac{\mathrm{D}}{\mathrm{D}t}\omega \,\mathrm{d}\sigma,\\ &= -\int_{R^2} \psi\frac{\partial\omega}{\partial t}\mathrm{d}\sigma = \nu_4\int_{R^2} \psi\Delta^2\omega \,\mathrm{d}\sigma - \nu_2\int_{R^2} \psi\Delta\omega \,\mathrm{d}\sigma,\\ &= -\nu_4\int_{R^2} |\nabla\omega|^2 \,\mathrm{d}\sigma - \nu_2\int_{R^2} \omega^2 \,\mathrm{d}\sigma, \qquad \text{(A 1)}\end{aligned}$$

Similarly we find for the change of enstrophy

$$\begin{aligned}\dot{Z} &= \frac{\mathrm{d}}{\mathrm{d}t}\int_{R^2}\omega^2\,\mathrm{d}\sigma = 2\int_{R^2}\omega\frac{\mathrm{D}\omega}{\mathrm{D}t}\mathrm{d}\sigma = 2\int_{R^2}\omega\frac{\partial\omega}{\partial t}\mathrm{d}\sigma,\\ &= 2\int_{R^2}\omega[-\nu_4\Delta^2\omega+\nu_2\Delta\omega]\,\mathrm{d}\sigma,\\ &= -2\nu_4\int_{R^2}(\Delta\omega)^2\,\mathrm{d}\sigma-2\nu_2\int_{R^2}(\nabla\omega)\cdot(\nabla\omega)\,\mathrm{d}\sigma. \end{aligned} \tag{A 2}$$

By introducing two lengthscales

$$\delta_2 \equiv \left[\int_{R^2}|\nabla\omega|^2\,\mathrm{d}\sigma/Z\right]^{-\frac{1}{2}} \tag{A 3}$$

and

$$\delta_4 \equiv \left[\int_{R^2}|\Delta\omega|^2\,\mathrm{d}\sigma/Z\right]^{-\frac{1}{4}} \tag{A 4}$$

we obtain the following decay laws from (A 1) and (A 2):

$$\tau_E \equiv -\frac{E}{\dot{E}} = \frac{E\delta_2^2}{2Z(\nu_4+\nu_2\delta_2^2)} \tag{A 5}$$

and

$$\tau_Z \equiv -\frac{Z}{\dot{Z}} = \frac{\delta_4^4\delta_2^2}{2(\nu_4\delta_2^2+\nu_2\delta_4^4)}. \tag{A 6}$$

Appendix B. A moment model with Newtonian viscosity, ν

The purpose of this Appendix is to generalize the moment model (Melander *et al.* 1986) to include a crude model of the Newtonian viscosity. The derivation follows the same lines as in the inviscid case, except for a few technical details.

From the evolution equation

$$\frac{\mathrm{D}\omega}{\mathrm{D}t} = \nu\Delta\omega \tag{B 1}$$

we find that for an arbitrary smooth function F

$$\begin{aligned}&\frac{\mathrm{d}}{\mathrm{d}t}\iint_{\mathbb{R}^2}F(x,y)\,\omega(x,y,t)\,\mathrm{d}x\,\mathrm{d}y\\ &= \iint_{\mathbb{R}^2}F(x,y)\frac{\mathrm{D}}{\mathrm{D}t}\omega(x,y,t)\,\mathrm{d}x\,\mathrm{d}y+\iint_{\mathbb{R}^2}\omega(x,y,t)\frac{\mathrm{D}}{\mathrm{D}t}F(x,y)\,\mathrm{d}x\,\mathrm{d}y\\ &= \nu\iint_{\mathbb{R}^2}F(x,y)\,\Delta\omega(x,y,t)\,\mathrm{d}x\,\mathrm{d}y+\iint_{\mathbb{R}^2}\omega(x,y,t)\,[F_x\psi_y-F_y\psi_x]\,\mathrm{d}x\,\mathrm{d}y\\ &= \nu\iint_{\mathbb{R}^2}\omega(x,y,t)\,\Delta F(x,y)\,\mathrm{d}x\,\mathrm{d}y+\iint_{\mathbb{R}^2}\omega(x,y,t)\,[F_x\psi_y-F_y\psi_x]\,\mathrm{d}x\,\mathrm{d}y,\end{aligned} \tag{B 2}$$

where ψ is the stream function as obtained from (7). We observe that the first term of (B 2) accounts for the viscous effects, while the second term of (B 2) is inviscid.

We assume that the vorticity is initially located in N well-separated uniform vortices. For nearly inviscid flows ($\nu \ll 1$) the vortices will remain nearly uniform for times much smaller than a typical diffusion timescale. We can therefore find regions $D_k, k = 1, 2, \dots, N$, each containing one vortex, such that these regions together account for essentially all the vorticity. By neglecting the vorticity outside these regions we find that the local physical space moments about the kth region's vorticity centroid (x_k, y_k),

$$J_k^{mn} = \iint_{D_k} (x-x_k)^m (y-y_k)^n \omega(x,y,t)\,\mathrm{d}x\,\mathrm{d}y, \tag{B 3}$$

obey the following equations

$$\dot{J}_k^{00} = 0, \tag{B 4}$$

$$\dot{J}_k^{10} = \iint_{D_k} \omega(x,y,t)\,\psi_y\,\mathrm{d}x\,\mathrm{d}y \equiv 0, \tag{B 5}$$

$$\dot{J}_k^{01} = -\iint_{D_k} \omega(x,y,t)\,\psi_x\,\mathrm{d}x\,\mathrm{d}y \equiv 0, \tag{B 6}$$

$$\dot{J}_k^{20} = 2\nu J_k^{00} + 2\iint_{D_k} \omega(x,y,t)\,(x-x_k)\,\psi_y\,\mathrm{d}x\,\mathrm{d}y, \tag{B 7}$$

$$\dot{J}_k^{11} = \iint_{D_k} \omega(x,y,t)\,((y-y_k)\,\psi_y - (x-x_k)\,\psi_x)\,\mathrm{d}x\,\mathrm{d}y, \tag{B 8}$$

$$\dot{J}_k^{02} = 2\nu J_k^{00} - 2\iint_{D_k} \omega(x,y,t)\,(y-y_k)\,\psi_x\,\mathrm{d}x\,\mathrm{d}y. \tag{B 9}$$

By arguments similar to those given in Melander *et al.* (1986) we exclude moments of order higher than two in order to obtain a model which is $O(\epsilon^3)$, where ϵ is defined in (13). The stream function ψ may be expressed in terms of the local moments in exactly the same way as in the inviscid case.

We now make the crude but simplifying assumption that the kth vortex can be modelled as an ellipse E_k with uniform vorticity $\bar{\omega}_k(t)$, that is

$$J_k^{mn}(t) = \bar{\omega}_k(t) \iint_{E_k} (x-x_k)^m (y-y_k)^n\,\mathrm{d}x\,\mathrm{d}y. \tag{B 10}$$

We can clearly restrict the class of permissible initial conditions such that (B 10) is satisfied at $t = 0$. Our goal then becomes to formulate evolution equations for $\bar{\omega}_k$ and the ellipse E_k as described by the centroid position (x_k, y_k), area A_k, aspect ratio λ_k and orientation ϕ_k.

From (B 4) we obtain

$$\dot{J}_k^{00} = \frac{\mathrm{d}}{\mathrm{d}t}\left[\bar{\omega}_k \iint_{E_k} \mathrm{d}x\,\mathrm{d}y\right] = \frac{\mathrm{d}}{\mathrm{d}t}[\bar{\omega}_k A_k] = 0; \tag{B 11}$$

thus the circulation Γ_k of each vortex is conserved. In order to determine $\dot{\bar{\omega}}_k$ and $\dot{A}_k$ we use the fact that for an ellipse with uniform vorticity

$$\frac{\Gamma_k^2 A_k^2}{16\pi^2} = \frac{\bar{\omega}_k^2 A_k^4}{16\pi^2} = J_k^{20} J_k^{02} - J_k^{11} J_k^{11}. \tag{B 12}$$

Differentiating with respect to time yields

$$A_k \dot{A}_k = \frac{8\pi^2}{\Gamma_k^2} J_k^{00}(J_k^{20}+J_k^{02}), \tag{B 13}$$

because the inviscid contributions cancel. When J_k^{mn} is expressed in terms of A_k, λ_k and ϕ_k we find from (B 13)

$$\dot{A}_k = 4\pi\nu \frac{1+\lambda_k^2}{\lambda_k}. \tag{B 14}$$

By the same technique we obtain from (B 12)

$$\dot{\bar{\omega}}_k = -\frac{4\pi\nu}{A_k}\bar{\omega}_k \frac{1+\lambda_k^2}{\lambda_k}. \tag{B 15}$$

(B 14) and (B 15) are easily seen to be consistent with (B 11). Thus we may substitute $\bar{\omega}_k$ by Γ_k/A_k.

From (B 2) we see that the evolution equations for the centroid positions governed only by the inviscid term. Therefore, we have from Melander *et al.* (1986), formula (3.25)

$$\begin{pmatrix} \dot{x} \\ \dot{y}_k \end{pmatrix} = \sum_{\substack{\alpha=1 \\ \alpha \neq k}}^{N} \frac{\Gamma_\alpha}{2\pi R_{k\alpha}} \left\{ \begin{matrix} -\sin\theta_{k\alpha} \\ \cos\theta_{k\alpha} \end{matrix} + \frac{A_\alpha}{4\pi R_{k\alpha}^2}\frac{1-\lambda_\alpha^2}{\lambda_\alpha}\begin{pmatrix} \sin(3\theta_{k\alpha}-2\phi_\alpha) \\ -\cos(3\theta_{k\alpha}-2\phi_\alpha) \end{pmatrix} \right.$$
$$\left. + \frac{A_k}{4\pi R_{k\alpha}^2}\frac{1-\lambda_k^2}{\lambda_k}\begin{pmatrix} \sin(3\theta_{k\alpha}-2\phi_k) \\ -\cos(3\theta_{k\alpha}-2\phi_k) \end{pmatrix}\right\}, \tag{B 16}$$

where $R_{k\alpha}$ and $\theta_{k\alpha}$ are defined such that

$$\begin{pmatrix} x_k - x_\alpha \\ y_k - x_\alpha \end{pmatrix} = R_{k\alpha}\begin{pmatrix} \cos\theta_{k\alpha} \\ \sin\theta_{k\alpha} \end{pmatrix}.$$

We shall now derive equations governing $\dot{\lambda}_k$ and $\dot{\phi}_k$. The sum and difference of the main moments are

$$S_k = J_k^{20} + J_k^{02} = \frac{\Gamma_k A_k}{\lambda_k}\frac{1+\lambda_k^2}{\lambda_k} \tag{B 17}$$

and

$$D_k = J_k^{20} - J_k^{02} = -\frac{\Gamma_k A_k}{\lambda_k}\frac{1-\lambda_k^2}{\lambda_k}\cos 2\phi_k, \tag{B 18}$$

while

$$J_k^{11} = -\frac{\Gamma_k A_k}{8\pi\lambda_k}(1-\lambda_k^2)\sin 2\phi_k. \tag{B 19}$$

By differentiating S_k, D_k and J_k^{11} with respect to time and applying (B 7)–(B 9) we obtain

$$\dot{\lambda}_k = -\frac{4\pi\nu}{A_k}(\lambda_k^2-1) + \lambda_k \sum_{\alpha=1}^{N'} \frac{\Gamma_\alpha}{\pi R_{k\alpha}^2}\sin(2(\theta_{k\alpha}-\phi_k)), \tag{B 20}$$

and

$$\dot{\phi}_k = \frac{\Gamma_k}{A_k}\frac{\lambda_k}{(1+\lambda_k)^2} + \frac{1+\lambda_k^2}{1-\lambda_k^2}\sum_{\alpha=1}^{N}{}' \frac{\Gamma_\alpha}{2\pi R_{k\alpha}^2}\cos(2(\theta_{k\alpha}-\phi_k)). \tag{B 21}$$

The dissipative moment model consists of (B 14), (B 16), (B 20) and (B 21). Note that it differs from the inviscid model only through the time dependence of A_k (which is governed by (B 14)) and the first term in (B 20).

It is straightforward to see that the total angular impulse

$$M = \sum_{k=1}^{N} \Gamma_k \left[x_k^2 + y_k^2 + \frac{A_k}{4\pi} \frac{1+\lambda_k^2}{\lambda_k} \right]$$

obeys the Poincaré identity

$$\dot{M} = 4\nu\Gamma. \tag{B 22}$$

The excess energy decreases according to

$$\frac{\dot{H}}{t} = -\sum_{k=1}^{N} \nu\Gamma_k \omega_k \frac{(\lambda_k - 1)^2}{\lambda_k} \leqslant 0 \tag{B 23}$$

which is not the same decay rate as for the Navier–Stokes equations (see (A 5)).

REFERENCES

AREF, H. 1983 Integrable, chaotic, and turbulent vortex motion in two-dimensional flows. *Ann. Rev. Fluid Mech.* **15**, 345–389.

BASSETT, A. B. 1888 *A Treatise of Hydrodynamics*. Republished in 1961 by Dover.

BROWN, G. L. & ROSHKO, A. 1974 On density effects and large structure in turbulent mixing layers. *J. Fluid Mech.* **64**, 775–816.

CHRISTIANSEN, J. P. 1973 Numerical simulation of hydrodynamics by the method of point vortices. *J. Comput. Phys.* **13**, 363–379.

CHRISTIANSEN, J. P. & ZABUSKY, N. J. 1973 Instability, coalesence and fission of finite-area vortex structures. *J. Fluid Mech.* **61**, 219–243.

DRITSCHEL, D. G. 1985 The stability and energetics of corotating uniform vortices. *J. Fluid Mech.* **157**, 95–134.

DRITSCHEL, D. G. 1986 The nonlinear evolution of rotating configurations of uniform vorticity. *J. Fluid Mech.* **172**, 157–182.

FREYMUTH, P. 1966 On transition in a separated boundary layer. *J. Fluid Mech.* **25**, 683.

HAIDVOGEL, D. B. 1985 Particle dispersion and Lagrangian vorticity conservation in a model of β-plane turbulence. Unpublished manuscript.

MCWILLIAMS, J. C. 1984 The emergence of isolated vortices in turbulent flow. *J. Fluid Mech.* **146**, 21–43.

MELANDER, M. V., MCWILLIAMS, J. C. & ZABUSKY, N. J. 1987*a* Axisymmetrization and vorticity-gradient intensification of an isolated two-dimensional vortex through filamentation. *J. Fluid Mech.* **178**, 137.

MELANDER, M. V., ZABUSKY, N. J. & MCWILLIAMS, J. C. 1987*b* Asymmetric vortex merger in two dimensions: which vortex is "victorious"? *Phys. Fluids* **30**, 2610–2612.

MELANDER, M. V., ZABUSKY, N. J. & STYCZEK, A. S. 1986 A moment model for vortex interactions of the two-dimensional Euler equations. Part 1. Computational validation of a Hamiltonian elliptical representation. *J. Fluid Mech.* **167**, 95–116.

OVERMAN, E. A. & ZABUSKY, N. J. 1982 Evolution and merger of isolated vortex structures. *Phys. Fluids* **25**, 1297–1305.

PULLIN, D. J. & PHILLIPS, W. R. C. 1981 On a generalization of Kaden's problem. *J. Fluid Mech.* **104**, 45–53.

ROBERTS, K. V. & CHRISTIANSEN, J. P. 1972 Topics in computational fluid mechanics. *Comput. Phys. Comm.* **3**, 14.

ROSSOW, V. J. 1977 Convective merging of vortex cores in lift generated wakes. *J. Aircraft* **14**, 283–290.

SAFFMAN, P. G. & SZETO, R. 1980 Equilibrium shapes of a pair of equal uniform vortices. *Phys. Fluids* **23**, 2339–2342.

WINANT, C. D. & BROWAND, F. K. 1974 Vortex pairing: the mechanism of turbulent mixing layer growth at moderate Reynolds number. *J. Fluid Mech.* **63**, 237.

WU, H. M., OVERMAN, E. A. & ZABUSKY, N. J. 1984 Steady state solutions of the Euler equations in two dimensions. Rotating and translating V-states with limiting cases. I. Numerical results. *J. Comput. Phys.* **53**, 42–71.

ZABUSKY, N. J. & DEEM, G. S. 1971 Dynamical evolution of two-dimensional unstable shear flows. *J. Fluid Mech.* **47**, 353–379.

ZABUSKY, N. J., HUGHES, M. H. & ROBERTS, K. V. 1979 Contour dynamics for the Euler equations in two dimensions. *J. Comput. Phys.* **30**, 96–106.